A wave-propagation based generalized Lagrangian method for compressible multicomponent flow problems

Keh-Ming Shyue

Department of Mathematics, National Taiwan University, Taipei 106, Taiwan

E-mail address: shyue@math.ntu.edu.tw

Abstract

A simple Lagrange-like moving grid approach is developed for the efficient numerical resolution of inviscid compressible multicomponent flow problems with a stiffened gas equation of state in more than one space dimension. The algorithm uses a variant of the fluid-mixture formulation of equations (cf. K.-M. Shyue, An efficient shock-capturing algorithm for compressible multicomponent problems, J. Comput. Phys. 142 (1998) 208–242) that are written in the generalized curvilinear coordinate as a basis to the modeling of the numerically induced mixing between two different fluid components within a computationally logical rectangular grid cell. In the algorithm, the temporal evolution of the physical grid system is chosen to follow approximately to the underlying flow fields, and a set of geometric conservation laws is included to describe the basic motion of the grid metrics associated with the coordinate transformation between the physical and logical grid. A standard flux-based wave decomposition method devised by Bale *et al.* (D. Bale, R.J. LeVeque, S. Mitran, J.A. Rossmanith, A wave propagation method for conservation laws and balance laws with spatially varying flux functions, SIAM J. Sci. Comput. 24 (2002) 955–978) is employed to solve the proposed multicomponent model with the dimensional-splitting technique incorporated in the method for multidimensional problems. Several numerical results are presented in one and two space dimensions that show the feasibility of the algorithm to the improvement of numerical resolution of interfaces when it is applied to solve a sample class of problems of practical importance.

AMS: 65M06, 76L05, 76M20, 76T05

Keywords: Generalized Lagrangian method; Flux-based wave decomposition; Compressible multicomponent flow; Stiffened gas equation of state; Spatially varying fluxes

1 Introduction

Our goal of this paper is to present a simple moving grid approach for the efficient numerical resolution of multicomponent flow problems with general inviscid compressible materials in more than one space dimension. We consider a simplified two-fluid problem as an example for the basic method development, where the flow regime of interest is assumed to be homogeneous with no jumps in the pressure and velocity (the normal component of it) across a material interface that separates regions of two different fluid components in an $N_d \geq 1$ spatial domain. The algorithm uses the Euler equations of gas dynamics as a model system for the principal motion of each fluid component in that the conservation form of the equations in an N_d-dimensional Cartesian coordinate $\vec{X} = (x_1, x_2, \ldots, x_{N_d})$ and time t can be written as

$$\frac{\partial}{\partial t}\begin{bmatrix} \rho \\ \rho u_i \\ E \end{bmatrix} + \sum_{j=1}^{N_d} \frac{\partial}{\partial x_j}\begin{bmatrix} \rho u_j \\ \rho u_i u_j + p\delta_{ij} \\ E u_j + p u_j \end{bmatrix} = 0 \qquad \text{for} \quad i = 1, 2, \ldots, N_d, \tag{1}$$

where ρ, u_i, p, E, and δ_{ij} denote the density, the particle velocity in the x_i-direction, the pressure, the total energy, and the Kronecker delta function, respectively. To complete the model, a linearized version of the Mie-Grüneisen (*i.e.*, the linearly density-dependent stiffened gas) equation of state of the form

$$p(\rho, e) = (\gamma - 1)\,\rho e + (\rho - \rho_0)\,\mathcal{B} \tag{2}$$

is assumed for the fundamental characterization of the thermodynamic behavior of the fluid component of concerned (cf. [24, 31, 33, 34]). Here e, γ, ρ_0, and $\mathcal{B}$ are in turn the specific internal energy, the adiabatic constant ($\gamma > 1$), the reference density, and the reference speed of sound. With that, the reference pressure is defined by $p_0 = \rho_0\mathcal{B}/\gamma$, and we have $E = \rho e + \rho \sum_{j=1}^{N_d} u_j^2/2$ as usual.

To solve this homogeneous two-fluid problem numerically, one popular approach among them is to take a uniform Cartesian grid and employ a fluid-mixture type interface-capturing method proposed previously by the author (cf. [44, 45, 46, 48, 49]). In this approach, to model grid cells that contain more than one fluid component, the method may be based on a volume-fraction formulation of the model system that is formed by combining the Euler equations (1) for the basic conservative variables of the fluid mixtures and an additional set of the effective equations

$$\begin{aligned} \frac{\partial}{\partial t}\left(\frac{\rho\mathcal{B}}{\gamma - 1}\right) + \sum_{j=1}^{N_d} \frac{\partial}{\partial x_j}\left(\frac{\rho\mathcal{B}}{\gamma - 1} u_j\right) = 0, \\ \frac{\partial \alpha}{\partial t} + \sum_{j=1}^{N_d} u_j \frac{\partial \alpha}{\partial x_j} = 0, \end{aligned} \tag{3}$$

for the mixtures of the material-dependent variables $\rho\mathcal{B}/(\gamma - 1)$ and α, respectively. Here $\alpha \in [0, 1]$ denotes the volume fraction of the fluid component within a grid cell. It should be mentioned that the above effective equations are introduced in the method primarily for a direct computation of the pressure from the equation of state,

$$p = \left[E - \frac{\sum_{j=1}^{N_d} (\rho u_j)^2}{2\rho} + \left(\frac{\rho\mathcal{B}}{\gamma - 1}\right) - \sum_{\iota=1}^{2} \alpha_\iota \frac{\rho_{0\iota}\mathcal{B}_\iota}{\gamma_\iota - 1}\right] \Bigg/ \sum_{\iota=1}^{2} \frac{\alpha_\iota}{\gamma_\iota - 1}, \tag{4}$$

and are derived so as to ensure a consistent modeling of the energy equation near the interfaces where two or more fluid components are present in a grid cell, and also the fulfillment of the mass equation in the other single component regions, see [48] for the details. Note that in (4) we have set $\alpha_1 = \alpha$ and $\alpha_2 = 1 - \alpha$ for the volume fractions occupied by the fluid-component 1 and 2, in a respective manner, and the mixtures of γ and $\rho_0\mathcal{B} = \gamma p_0$ are computed by

$$\gamma = 1 + 1 \Bigg/ \sum_{\iota=1}^{2} \frac{\alpha_\iota}{\gamma_\iota - 1} \qquad \text{and} \qquad \rho_0\mathcal{B} = \sum_{\iota=1}^{2} \alpha_\iota \frac{\rho_{0\iota}\mathcal{B}_\iota}{\gamma_\iota - 1} \Bigg/ \sum_{\iota=1}^{2} \frac{\alpha_\iota}{\gamma_\iota - 1}.$$

A standard high-resolution wave propagation method (cf. [26]) can then be used to find approximate solutions of the model system for multicomponent problems, yielding results that are free of spurious oscillations in the pressure near a somewhat smeared interface, see Section 6 for an example.

In this work, motivated by the success of a unified coordinate approach advocated by Hui and coworkers for single component flow problems with interfaces and complex geometries (cf. [16, 17, 18, 19]), we are interested in a novel moving grid method that is a generalization of the aforementioned fluid-mixture method and is also an easy extension of the unified coordinate approach for multicomponent flows. Here as a first endeavor, we focus our attention on the improved numerical resolution of interfaces, but leave the problems with complex geometries in a sequel. In this instance, a simple Lagrange-like condition of the form

$$\frac{\partial \vec{X}}{\partial t} = h\vec{u} \tag{5}$$

is assumed as the basis for the temporal evolution of the physical grid coordinate $\vec{X}$, where $\vec{u} = (u_1, u_2, \ldots, u_{Nd})$ is the vector of the particle velocity, and $h \in [0, 1]$ is a freely chosen parameter that takes on the value of zero when we have a fixed Eulerian grid, and on the value of unity when we have a Lagrangian grid, see [5, 9, 28, 29, 30, 41] and the references cited therein for some background information of a Lagrangian-type method. Note that, in practice, we have chosen a fixed constant $h = 0.99$ in almost all the numerical tests carried out in Section 6, but do not consider the more general space- and time-dependent case (cf. [17, 19, 20]) in the present study.

With the mesh-moving condition (5), the algorithm employs a variant of the model equations (1) and (3) that are written in a generalized curvilinear coordinate as a basis to the modeling of the numerically induced mixing between two different fluid components within a computational (logical) rectangular grid cell. In addition to that, a set of geometric conservation laws is included to describe the basic motion of the grid metrics associated with the coordinate transformation between the physical and computational grid. This will be described further in Section 2.

We use a finite volume method based on an f-waves decomposition viewpoint developed by Bale *et al.* [2] to find approximate solutions of our proposed multicomponent model in generalized coordinates with the dimensional-splitting technique incorporated in the method for multidimensional problems. The method is a variant of the Godunov scheme, and has been widely used in many applications including the single-component fluid of ideal gases on general quadrilateral grids [26], and hyperbolic systems on curved manifolds [40] and on spheres [39]. The current use of the method extends the previous one from a single-component to multicomponent problems and also from the equations to be solved in the Cartesian coordinate in the physical space to the generalized coordinate in the logical space. It is an efficient and yet accurate scheme without introducing any spurious oscillations in the pressure near an interface as illustrated by numerical results presented in this paper. The basic idea of this method will be reviewed briefly in Section 4.

It should be mentioned that due to the Lagrangian nature of the above moving grid condition in problems when there is a large interfacial deformation or collapse of the underlying velocity field into a narrow region (cf.[46, 50]), for example, the grid system that is generated by the algorithm during the computation would be suffering from the usual grid tangling and so eventually the break down of the method in some instances. Despite this, there are some problems of sufficient interest that the current approach is worthwhile, particularly since it is relatively easy to implement the method in more than one space dimension and can provide a better resolution of interfaces than standard Eulerian methods. Moreover, the methodology we have proposed here can be extended quite straightforwardly to problems involving more than two fluid components and more complicated equations of state. Without going into the details for that, our goal is to establish the basic solution strategy and validate its use via some sample numerical experimentations.

This paper is organized as follows. In Section 2, we describe our mathematical model for the present homogeneous two-fluid problems in a generalized curvilinear coordinate. In Section 3, we discuss the hyperbolicity of the proposed model equations. In Section 4, we give a brief review of the dimensional-splitting version of the high-resolution flux-based wave decomposition method for multi-dimensional problems. In Section 5, we explain the Riemann problem and a shock-only Riemann solver that is fundamental in our algorithm for numerical approximation. Numerical results of some sample examples in one and two space dimensions are presented in Section 6.

2 Mathematical models in generalized coordinates

We begin our discussion by describing a general coordinate transformation of the aforementioned fluid-mixture type model system, *i.e.*, the combined equations (1) and (3), from the Cartesian coordinate

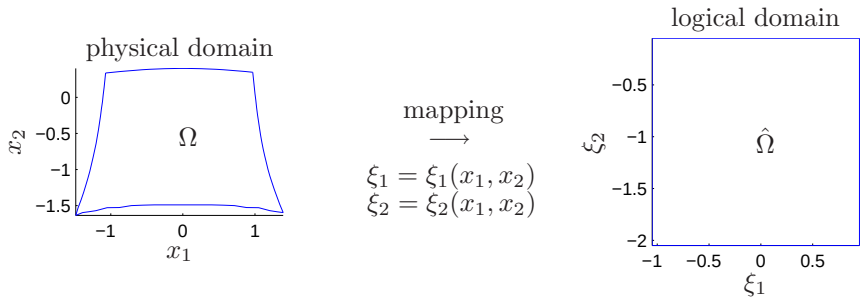

Figure 1: An example of a general non-rectangular domain Ω in two dimensions on the left that is mapped to a logical domain $\hat{\Omega}$ on the right via the transformation (6).

$\vec{X} = (x_1, x_2, \ldots, x_{N_d})$ in a physical domain Ω to the generalized coordinate $\vec{\Xi} = (\xi_1, \xi_2, \ldots, \xi_{N_d})$ in a computationally logical domain $\hat{\Omega}$ via the relations

$$\tau = t, \qquad \xi_j = \xi_j(\vec{X}, t) \qquad \text{for } j = 1, 2, \ldots, N_d \tag{6}$$

that is fundamental in our moving grid algorithm for constructing approximate solutions of the present homogeneous two-fluid problems with the stiffened gas equation of state (2), see Fig. 1 for an illustration of the spatial domain of interest when $N_d = 2$. In this instance, using the chain rule of partial differentiation, we have

$$\begin{aligned} \frac{\partial}{\partial t} &= \frac{\partial}{\partial \tau} + \sum_{i=1}^{N_d} \frac{\partial \xi_i}{\partial t} \frac{\partial}{\partial \xi_i}, \\ \frac{\partial}{\partial x_j} &= \sum_{i=1}^{N_d} \frac{\partial \xi_i}{\partial x_j} \frac{\partial}{\partial \xi_i} \qquad \text{for } j = 1, 2, \ldots, N_d. \end{aligned} \tag{7}$$

Here $\partial \xi_i / \partial t$ and $\partial \xi_i / \partial x_j$ appearing in the above equations for $i, j = 1, 2, \ldots, N_d$, are the so-called metrics, and have $N_d(N_d+1)$ of them in total. For computational purposes, it is often desirable to find expressions that relate the above metrics in the logical domain to the derivatives in the physical domain. We can do this quite straightforwardly (cf. [1, 15, 54]) if the existence of the inverse transformation of (6) is assumed, *i.e.*,

$$t = \tau, \qquad x_j = x_j(\vec{\Xi}, t) \qquad \text{for } j = 1, 2, \ldots, N_d, \tag{8}$$

and the elementary differential rule from multi variable calculus as

$$\frac{\partial(\tau, \vec{\Xi})}{\partial(t, \vec{X})} = \frac{\partial(t, \vec{X})}{\partial(\tau, \vec{\Xi})}^{-1} \tag{9}$$

is used in the derivation. Note that in matrix form $\partial(\tau, \vec{\Xi})/\partial(t, \vec{X})$ and $\partial(t, \vec{X})/\partial(\tau, \vec{\Xi})$ are given by

$$\begin{pmatrix} 1 & 0 & \ldots & 0 \\ \partial_t \xi_1 & \partial_{x_1} \xi_1 & \ldots & \partial_{x_{N_d}} \xi_1 \\ \partial_t \xi_2 & \partial_{x_1} \xi_2 & \ldots & \partial_{x_{N_d}} \xi_2 \\ \vdots & \vdots & \vdots & \vdots \\ \partial_t \xi_{N_d} & \partial_{x_1} \xi_{N_d} & \ldots & \partial_{x_{N_d}} \xi_{N_d} \end{pmatrix} \quad \text{and} \quad \begin{pmatrix} 1 & 0 & \ldots & 0 \\ \partial_\tau x_1 & \partial_{\xi_1} x_1 & \ldots & \partial_{\xi_{N_d}} x_1 \\ \partial_\tau x_2 & \partial_{\xi_1} x_2 & \ldots & \partial_{\xi_{N_d}} x_2 \\ \vdots & \vdots & \vdots & \vdots \\ \partial_\tau x_{N_d} & \partial_{\xi_1} x_{N_d} & \ldots & \partial_{\xi_{N_d}} x_{N_d} \end{pmatrix},$$

respectively, where to simplify the presentation we have used the notation $\partial_a z = \partial z / \partial a$ for any pair of variables z and a.

As an example, we consider the three-dimensional case $N_d = 3$, and so from (9) we would have

$$\begin{pmatrix} 1 & 0 & 0 & 0 \\ \partial_t\xi_1 & \partial_{x_1}\xi_1 & \partial_{x_2}\xi_1 & \partial_{x_3}\xi_1 \\ \partial_t\xi_2 & \partial_{x_1}\xi_2 & \partial_{x_2}\xi_2 & \partial_{x_3}\xi_2 \\ \partial_t\xi_3 & \partial_{x_1}\xi_3 & \partial_{x_2}\xi_3 & \partial_{x_3}\xi_3 \end{pmatrix} = \begin{pmatrix} 1 & 0 & 0 & 0 \\ \partial_\tau x_1 & \partial_{\xi_1} x_1 & \partial_{\xi_2} x_1 & \partial_{\xi_3} x_1 \\ \partial_\tau x_2 & \partial_{\xi_1} x_2 & \partial_{\xi_2} x_2 & \partial_{\xi_3} x_2 \\ \partial_\tau x_3 & \partial_{\xi_1} x_3 & \partial_{\xi_2} x_3 & \partial_{\xi_3} x_3 \end{pmatrix}^{-1} = \frac{1}{J}\begin{pmatrix} J & 0 & 0 & 0 \\ J_{01} & J_{11} & J_{21} & J_{31} \\ J_{02} & J_{12} & J_{22} & J_{32} \\ J_{03} & J_{13} & J_{23} & J_{33} \end{pmatrix},$$

where $J = |\partial(x_1, x_2, x_3)/\partial(\xi_1, \xi_2, \xi_3)|$ is the determinant of the matrix $\partial(x_1, x_2, x_3)/\partial(\xi_1, \xi_2, \xi_3)$, and J_{ij} for $i, j = 1, 2, 3$, are the entries satisfying the following expressions:

$$\begin{aligned} J_{11} &= |\partial(x_2, x_3)/\partial(\xi_2, \xi_3)|\,, \quad J_{21} = |\partial(x_1, x_3)/\partial(\xi_3, \xi_2)|\,, \quad J_{31} = |\partial(x_1, x_2)/\partial(\xi_2, \xi_3)|\,, \\ J_{12} &= |\partial(x_2, x_3)/\partial(\xi_3, \xi_1)|\,, \quad J_{22} = |\partial(x_1, x_3)/\partial(\xi_1, \xi_3)|\,, \quad J_{32} = |\partial(x_1, x_2)/\partial(\xi_3, \xi_1)|\,, \\ J_{13} &= |\partial(x_2, x_3)/\partial(\xi_1, \xi_2)|\,, \quad J_{23} = |\partial(x_1, x_3)/\partial(\xi_2, \xi_1)|\,, \quad J_{33} = |\partial(x_1, x_2)/\partial(\xi_1, \xi_2)|\,. \end{aligned}$$

In addition to that, we also have $J_{0j} = -\sum_{i=1}^{N_d} J_{ij}\partial_\tau x_i$, $j = 1, 2, 3$. Now the metrics in (7) which consist of twelve spatial- and temporal-varying quantities in a three-dimensional logical domain may take the form

$$D\xi_j = \left(\partial_t\xi_j,\ \nabla_{\vec{X}}\xi_j\right) = \left(\partial_t\xi_j,\ \partial_{x_1}\xi_j,\ \partial_{x_2}\xi_j,\ \partial_{x_3}\xi_j\right) = \frac{1}{J}\left(J_{0j},\ J_{1j},\ J_{2j},\ J_{3j}\right) \tag{10}$$

for $j = 1, 2, 3$, that are conveniently dependent on the derivatives in the physical domain.

With these definitions, after some simple algebraic manipulations (cf. [15]), the transformed version of our two-fluid model in the logical domain $\hat{\Omega}$ can be written as

$$\begin{aligned} \frac{\partial}{\partial\tau}\left(\rho J\right) + \sum_{j=1}^{N_d}\frac{\partial}{\partial\xi_j}\left(\rho J U_j\right) &= 0, \\ \frac{\partial}{\partial\tau}\left(\rho J u_i\right) + \sum_{j=1}^{N_d}\frac{\partial}{\partial\xi_j} J\left(\rho u_i U_j + p\frac{\partial\xi_j}{\partial x_i}\right) &= 0 \qquad \text{for} \quad i = 1, 2, \ldots, N_d, \\ \frac{\partial}{\partial\tau}\left(JE\right) + \sum_{j=1}^{N_d}\frac{\partial}{\partial\xi_j} J\left(EU_j + pU_j - p\frac{\partial\xi_j}{\partial t}\right) &= 0, \\ \frac{\partial}{\partial\tau}\left(\frac{\rho\mathcal{B}}{\gamma-1}J\right) + \sum_{j=1}^{N_d}\frac{\partial}{\partial\xi_j}\left(\frac{\rho\mathcal{B}}{\gamma-1}JU_j\right) &= 0, \\ \frac{\partial\alpha}{\partial\tau} + \sum_{j=1}^{N_d} U_j\frac{\partial\alpha}{\partial\xi_j} &= 0, \end{aligned} \tag{11}$$

where $U_j = \partial_t\xi_j + \sum_{i=1}^{N_d} u_i\partial_{x_i}\xi_j$ denotes the contravariant velocity in the ξ_j-direction for $j = 1, 2, \ldots, N_d$. It is clear that in this system the first $N_d + 2$ are simply the compressible Euler equations in strong conservation-law form, while the remaining are the effective equations that are introduced to ensure the correct mixing of the problem-dependent material variables near the interfaces. It is easy to observe also that the flux functions of the conservation laws in the transformed model depend not only on the conserved variables but also on the spatially-varying metrics which is unlike the case in the original model where the fluxes are dependent on the conserved variables only. We should have this in mind when we want to develop a method that discretizes the model for numerical approximation.

It is important to note that in the general $\partial\vec{X}/\partial t \neq 0$ case of (5), to complete the model, we have to devise a way for the numerical resolution of the metrics that are presence in (11) throughout the computations. Among a wide variety of methodologies proposed in the literature (cf. [1, 9, 21, 30, 32, 53]),

in this work, we are interested in an approach that is based on the compatibility condition of the mixed second order partial derivatives $\partial_\tau \partial_{\xi_j} x_i$ and $\partial_{\xi_j} \partial_\tau x_i$ to yield the geometric conservation laws of the form

$$\frac{\partial}{\partial \tau}\left(\frac{\partial x_i}{\partial \xi_j}\right) + \frac{\partial}{\partial \xi_j}\left(-\frac{\partial x_i}{\partial \tau}\right) = 0 \qquad \text{for } i, j = 1, 2, \ldots, N_d.$$

This approach has been used quite successfully in a unified coordinate method (cf.[16, 17, 19]) for solving general fluid flow problems with stationary or moving complex geometries and also in a Lagrangian scheme for gas dynamics (cf. [9]). It is a simple way to be coped with our current implementation of a dimension-by-dimension splitting method described in Section 4 for numerical approximation of multi-dimensional problems. Note that, to avoid any possible confusion that may cause in the above equations, we introduce a new set of notation $\chi_{ji} = \partial_{\xi_j} x_i$ as for the unknowns (N_d^2 of them in total for $i, j = 1, 2, \ldots, N_d$) and when combining the mesh-moving relation (5) for $\partial_\tau x_i$ in the problem formulation, we therefore have

$$\frac{\partial \chi_{ji}}{\partial \tau} + \frac{\partial}{\partial \xi_j}\left(-h u_i\right) = 0 \qquad \text{for } i, j = 1, 2, \ldots, N_d. \tag{12}$$

It is certain that, with a prescribed region of the physical domain for the computation (rectangular or not), the initial grid system and also the initial condition of the above equations can be obtained by a chosen technique from numerical grid generators (cf. [4, 54]) when it is necessary. Once the solutions of (12) are known during a time step, it is an easy manner to compute the various determinants that are required in (10) for the metrics.

In summary, together with the stiffened gas equation of state (2) and the Lagrange-like moving grid condition (5), the model equations we propose to solve compressible homogeneous two-fluid problems consist of the physical part (11) and the geometrical part (12); this gives us totally $N_d^2 + N_d + 4$ equations to be solved in an N_d spatial (logical) domain. Surely, when h approaches to zero, this model reduces to the physical part (11) only. With a model system formulated in this way, there is no difficulty to compute the pressure from the equation of state (4) in the entire computational region at all time.

For the ease of the later reference, this two-fluid model is written in the following form

$$\frac{\partial q}{\partial \tau} + \sum_{j=1}^{N_d} f_j\left(\frac{\partial}{\partial \xi_j}, q\right) = 0, \tag{13}$$

where in the two-dimensional case $N_d = 2$, for example, the state vector q and the vector-value functions f_1, f_2 are defined by

$$q = \left[\rho J,\ \rho J u_1,\ \rho J u_2,\ EJ,\ \frac{\rho \mathcal{B}}{\gamma - 1} J,\ \alpha,\ \chi_{11},\ \chi_{12},\ \chi_{21},\ \chi_{22}\right]^T, \tag{14a}$$

$$\begin{aligned} f_1 = \Bigg[&\frac{\partial}{\partial \xi_1}\left(\rho J U_1\right),\ \frac{\partial}{\partial \xi_1}\left(\rho J u_1 U_1 + p\chi_{22}\right),\ \frac{\partial}{\partial \xi_1}\left(\rho J u_2 U_1 - p\chi_{21}\right),\ \frac{\partial}{\partial \xi_1}(EJU_1 + \\ &p(u_1\chi_{22} - u_2\chi_{21})),\ \frac{\partial}{\partial \xi_1}\left(\frac{\rho \mathcal{B}}{\gamma - 1} J U_1\right),\ U_1 \frac{\partial \alpha}{\partial \xi_1},\ \frac{\partial}{\partial \xi_1}\left(-h u_1\right),\ \frac{\partial}{\partial \xi_1}\left(-h u_2\right),\ 0,\ 0\Bigg]^T, \end{aligned} \tag{14b}$$

and

$$\begin{aligned} f_2 = \Bigg[&\frac{\partial}{\partial \xi_2}\left(\rho J U_2\right),\ \frac{\partial}{\partial \xi_2}\left(\rho J u_1 U_2 - p\chi_{12}\right),\ \frac{\partial}{\partial \xi_2}\left(\rho J u_2 U_2 + p\chi_{11}\right),\ \frac{\partial}{\partial \xi_2}(EJU_2 + \\ &p(u_2\chi_{11} - u_1\chi_{12})),\ \frac{\partial}{\partial \xi_2}\left(\frac{\rho \mathcal{B}}{\gamma - 1} J U_2\right),\ U_2 \frac{\partial \alpha}{\partial \xi_2},\ 0,\ 0,\ \frac{\partial}{\partial \xi_2}\left(-h u_1\right),\ \frac{\partial}{\partial \xi_2}\left(-h u_2\right)\Bigg]^T, \end{aligned} \tag{14c}$$

in a respective manner, with

$$\begin{aligned} U_1 &= (1-h)(u_1\chi_{22} - u_2\chi_{21})/J, \\ U_2 &= (1-h)(u_2\chi_{11} - u_1\chi_{12})/J, \end{aligned} \tag{15}$$

and $J = \chi_{11}\chi_{22} - \chi_{21}\chi_{22}$. Note that when $h \neq 1$, the proposed system is not written in the full conservation form, but is rather a quasi-conservative system of equations. In the special Lagrangian case where $h = 1$, however, we have a conservative system where (14b) is simplified to

$$f_1 = \left[0,\ \frac{\partial p\chi_{22}}{\partial \xi_1},\ -\frac{\partial p\chi_{21}}{\partial \xi_1},\ \frac{\partial}{\partial \xi_1}p(u_1\chi_{22} - u_2\chi_{21}),\ 0,\ 0,\ -\frac{\partial u_1}{\partial \xi_1},\ -\frac{\partial u_2}{\partial \xi_1},\ 0,\ 0\right]^T, \tag{16a}$$

and (14c) is simplified to

$$f_2 = \left[0,\ -\frac{\partial p\chi_{12}}{\partial \xi_2},\ \frac{\partial p\chi_{11}}{\partial \xi_2},\ \frac{\partial}{\partial \xi_2}p(u_2\chi_{11} - u_1\chi_{12}),\ 0,\ 0,\ 0,\ 0,\ -\frac{\partial u_1}{\partial \xi_2},\ -\frac{\partial u_2}{\partial \xi_2}\right]^T, \tag{16b}$$

see [9] for an alternative and yet interesting form of the Lagrangian system when the additional constraints:

$$\frac{\partial \chi_{21}}{\partial \xi_1} = \frac{\partial \chi_{11}}{\partial \xi_2} \qquad \text{and} \qquad \frac{\partial \chi_{22}}{\partial \xi_1} = \frac{\partial \chi_{12}}{\partial \xi_2},$$

are being imposed in the mathematical formulation.

In addition, we use the notations $\breve{f}_\iota$ to denote the flux functions for the conservation laws of (13) in the ξ_ι-direction, yielding

$$\begin{aligned} \breve{f}_1 = \Big[&\rho J U_1,\ \rho J u_1 U_1 + p\chi_{22},\ \rho J u_2 U_1 - p\chi_{21},\ EJU_1 + p(u_1\chi_{22} - u_2\chi_{21}),\ \frac{\rho\mathcal{B}}{\gamma-1}JU_1, \\ &0,\ -hu_1,\ -hu_2,\ 0,\ 0\Big]^T \end{aligned} \tag{17a}$$

for the fluxes in the ξ_1-direction, and

$$\begin{aligned} \breve{f}_2 = \Big[&\rho J U_2,\ \rho J u_1 U_2 - p\chi_{12},\ \rho J u_2 U_2 + p\chi_{11},\ EJU_2 + p(u_2\chi_{11} - u_1\chi_{12}),\ \frac{\rho\mathcal{B}}{\gamma-1}JU_2, \\ &0,\ 0,\ 0,\ -hu_1,\ -hu_2\Big]^T \end{aligned} \tag{17b}$$

for the fluxes in the ξ_2-direction when $N_d = 2$.

3 Hyperbolicity of the model equations

To examine the hyperbolicity of (13), it is a common practice to inquire the characteristic structure of the quasi-linear form of the equations

$$\frac{\partial q}{\partial \tau} + \sum_{j=1}^{N_d} A_j(q)\frac{\partial q}{\partial \xi_j} = 0, \tag{18}$$

when the proper smoothness of the solutions is assumed. Without loss of generality, we consider the two-dimensional case $N_d = 2$ as an example, and so have the state vector q in (18) defined by (14a) and the matrices A_j for $j = 1, 2$ that are derived from (14b) and (14c), respectively, to be of the form

$$A_j = \left[A_{j,1},\ A_{j,2},\ \ldots,\ A_{j,9},\ A_{j,10}\right]$$

with $A_{j,m}$, $m = 1, 2, \ldots, 10$, denoting the mth row vector for matrix A_j. Here, for matrix A_1, we have

$$A_{1,1} = \left[0,\ \frac{(1-h)\chi_{22}}{J},\ -\frac{(1-h)\chi_{21}}{J},\ 0,\ 0,\ 0,\ -\rho U_1\chi_{22},\ \rho U_1\chi_{21},\ -\rho U_2\chi_{22},\ \rho U_2\chi_{21}\right],$$

$$\begin{aligned}
A_{1,2} = \Bigg[&\frac{K\chi_{22}}{J} - u_1U_1,\ \frac{u_1(1-h-\Gamma)\chi_{22}}{J} + U_1,\ -\frac{u_1(1-h)\chi_{21}}{J} - \frac{u_2\Gamma\chi_{22}}{J},\ \frac{\Gamma\chi_{22}}{J},\ \frac{\Gamma\chi_{22}}{J},\\
&\varphi\chi_{22},\ -\left(\rho u_1U_1 + \frac{(p+\rho_0\mathcal{B})\chi_{22}}{J}\right)\chi_{22},\ \left(\rho u_1U_1 + \frac{(p+\rho_0\mathcal{B})\chi_{22}}{J}\right)\chi_{21},\\
&-\left(\rho u_1U_2 - \frac{(p+\rho_0\mathcal{B})\chi_{12}}{J}\right)\chi_{22},\ \left(\rho u_1U_2 - \frac{(p+\rho_0\mathcal{B})\chi_{12}}{J}\right)\chi_{21} - \rho_0\mathcal{B}\Bigg],\\
A_{1,3} = \Bigg[&-\frac{K\chi_{21}}{J} - u_2U_1,\ \frac{u_2(1-h)\chi_{22}}{J} + \frac{u_1\Gamma\chi_{21}}{J},\ -\frac{u_2(1-h-\Gamma)\chi_{21}}{J} + U_1,\ -\frac{\Gamma\chi_{21}}{J},\ -\frac{\Gamma\chi_{21}}{J},\\
&-\varphi\chi_{21},\ -\left(\rho u_2U_1 - \frac{(p+\rho_0\mathcal{B})\chi_{21}}{J}\right)\chi_{22},\ \left(\rho u_2U_1 - \frac{(p+\rho_0\mathcal{B})\chi_{21}}{J}\right)\chi_{21},\\
&-\left(\rho u_2U_2 + \frac{(p+\rho_0\mathcal{B})\chi_{11}}{J}\right)\chi_{22} + \rho_0\mathcal{B},\ \left(\rho u_2U_2 + \frac{(p+\rho_0\mathcal{B})\chi_{11}}{J}\right)\chi_{21}\Bigg],\\
A_{1,4} = \Bigg[&(K-M)V_1,\ \frac{M\chi_{22}}{J} - u_1V_1\Gamma,\ -\frac{M\chi_{21}}{J} - u_2V_1\Gamma,\ (1-h+\Gamma)V_1,\ \Gamma V_1,\ \varphi V_1,\\
&-(\rho M + \rho_0\mathcal{B})V_1\chi_{22},\ (\rho M + \rho_0\mathcal{B})V_1\chi_{21},\ -(\rho M + \rho_0\mathcal{B})V_2\chi_{22} + \rho_0\mathcal{B}u_2,\\
&(\rho M + \rho_0\mathcal{B})V_2\chi_{21} - \rho_0\mathcal{B}u_1\Bigg],\\
A_{1,5} = \Bigg[&-\frac{\mathcal{B}U_1}{\Gamma},\ \frac{\mathcal{B}(1-h)\chi_{22}}{\Gamma J},\ -\frac{\mathcal{B}(1-h)\chi_{21}}{\Gamma J},\ 0,\ U_1,\ 0,\ -\frac{\rho\mathcal{B}U_1\chi_{22}}{\Gamma},\ \frac{\rho\mathcal{B}U_1\chi_{21}}{\Gamma},\\
&-\frac{\rho\mathcal{B}U_2\chi_{22}}{\Gamma},\ \frac{\rho\mathcal{B}U_2\chi_{21}}{\Gamma}\Bigg],\\
A_{1,6} = &\left[0,\ 0,\ 0,\ 0,\ 0,\ U_1,\ 0,\ 0,\ 0,\ 0\right],\\
A_{1,7} = &\left[\frac{u_1h}{\rho J},\ -\frac{h}{\rho J},\ 0,\ 0,\ 0,\ 0,\ 0,\ 0,\ 0,\ 0\right],\\
A_{1,8} = &\left[\frac{u_2h}{\rho J},\ 0,\ -\frac{h}{\rho J},\ 0,\ 0,\ 0,\ 0,\ 0,\ 0,\ 0\right],\\
A_{1,9} = &\ 0,\\
A_{1,10} = &\ 0,
\end{aligned}$$

and for matrix A_2, we have

$$\begin{aligned}
A_{2,1} = \Bigg[&0,\ -\frac{(1-h)\chi_{12}}{J},\ \frac{(1-h)\chi_{11}}{J},\ 0,\ 0,\ 0,\ \rho U_1\chi_{12},\ -\rho U_1\chi_{11},\ \rho U_2\chi_{12},\ -\rho U_2\chi_{11}\Bigg],\\
A_{2,2} = \Bigg[&-\frac{K\chi_{12}}{J} - u_1U_2,\ -\frac{u_1(1-h-\Gamma)\chi_{12}}{J} + U_2,\ \frac{u_1(1-h)\chi_{11}}{J} + \frac{u_2\Gamma\chi_{12}}{J},\ -\frac{\Gamma\chi_{12}}{J},\ -\frac{\Gamma\chi_{12}}{J},\\
&-\varphi\chi_{12},\ \left(\rho u_1U_1 + \frac{(p+\rho_0\mathcal{B})\chi_{22}}{J}\right)\chi_{12},\ -\left(\rho u_1U_1 + \frac{(p+\rho_0\mathcal{B})\chi_{22}}{J}\right)\chi_{11} + \rho_0\mathcal{B},\\
&\left(\rho u_1U_2 - \frac{(p+\rho_0\mathcal{B})\chi_{12}}{J}\right)\chi_{12},\ -\left(\rho u_1U_2 - \frac{(p+\rho_0\mathcal{B})\chi_{12}}{J}\right)\chi_{11}\Bigg],
\end{aligned}$$

$$
\begin{aligned}
A_{2,3} = \Bigg[& \frac{K\chi_{11}}{J} - u_2U_2,\ -\frac{u_2(1-h)\chi_{12}}{J} - \frac{u_1\Gamma\chi_{11}}{J},\ \frac{u_2(1-h-\Gamma)\chi_{11}}{J} + U_2,\ \frac{\Gamma\chi_{11}}{J},\ \frac{\Gamma\chi_{11}}{J}, \\
& \varphi\chi_{11},\ \left(\rho u_2U_1 - \frac{(p+\rho_0\mathcal{B})\chi_{21}}{J}\right)\chi_{12} - \rho_0\mathcal{B},\ -\left(\rho u_2U_1 - \frac{(p+\rho_0\mathcal{B})\chi_{21}}{J}\right)\chi_{11}, \\
& \left(\rho u_2U_2 + \frac{(p+\rho_0\mathcal{B})\chi_{11}}{J}\right)\chi_{12},\ -\left(\rho u_2U_2 + \frac{(p+\rho_0\mathcal{B})\chi_{11}}{J}\right)\chi_{11}\Bigg], \\
A_{2,4} = \Bigg[& (K-M)V_2,\ -\frac{M\chi_{12}}{J} - u_1V_2\Gamma,\ \frac{M\chi_{11}}{J} - u_2V_2\Gamma,\ (1-h+\Gamma)V_2,\ \Gamma V_2,\ \varphi V_2, \\
& (\rho M + \rho_0\mathcal{B})V_1\chi_{12} - \rho_0\mathcal{B}u_2,\ -(\rho M + \rho_0\mathcal{B})V_1\chi_{11} + \rho_0\mathcal{B}u_1,\ (\rho M + \rho_0\mathcal{B})V_2\chi_{12}, \\
& -(\rho M + \rho_0\mathcal{B})V_2\chi_{11}\Bigg], \\
A_{2,5} = \Bigg[& -\frac{\mathcal{B}U_2}{\Gamma},\ -\frac{\mathcal{B}(1-h)\chi_{12}}{\Gamma J},\ \frac{\mathcal{B}(1-h)\chi_{11}}{\Gamma J},\ 0,\ U_2,\ 0,\ \frac{\rho\mathcal{B}U_1\chi_{12}}{\Gamma},\ -\frac{\rho\mathcal{B}U_1\chi_{11}}{\Gamma}, \\
& \frac{\rho\mathcal{B}U_2\chi_{12}}{\Gamma},\ -\frac{\rho\mathcal{B}U_2\chi_{11}}{\Gamma}\Bigg], \\
A_{2,6} = & \left[0,\ 0,\ 0,\ 0,\ 0,\ U_2,\ 0,\ 0,\ 0,\ 0\right], \\
A_{2,7} = & \ 0, \\
A_{2,8} = & \ 0, \\
A_{2,9} = & \left[\frac{u_1h}{\rho J},\ -\frac{h}{\rho J},\ 0,\ 0,\ 0,\ 0,\ 0,\ 0,\ 0,\ 0\right], \\
A_{2,10} = & \left[\frac{u_2h}{\rho J},\ 0,\ -\frac{h}{\rho J},\ 0,\ 0,\ 0,\ 0,\ 0,\ 0,\ 0\right].
\end{aligned}
$$

Note that in the above matrix entries we have used the following notations for abbreviation: $\Gamma = \gamma - 1$, $K = \Gamma(u_1^2 + u_2^2)/2$, $M = ((1-h)E + p)/\rho$, $V_1 = \vec{u}\cdot\nabla_{\vec{X}}\xi_1 = (u_1\chi_{22} - u_2\chi_{21})/J$, $V_2 = \vec{u}\cdot\nabla_{\vec{X}}\xi_2 = (u_2\chi_{11} - u_1\chi_{12})/J$, and $\varphi = -\Gamma[(p+\rho_{01}\mathcal{B}_1)/(\gamma_1 - 1) - (p+\rho_{02}\mathcal{B}_2)/(\gamma_2 - 1)]$.

Before proceeding further, we recall that, for any given N_d, a nonlinear system of partial differential equations of the form (13) is said to be (strongly) hyperbolic if any linear combination of the matrices A_j for $j = 1, 2, \ldots, N_d$ appearing in (18) has (i) real eigenvalues and (ii) a complete set of linearly independent right eigenvectors. It is said to be weakly hyperbolic if (i) is satisfied but (ii) is not fulfilled due to the presence of a Jordan block (cf. [13, 23]).

Now let $\vec{n}_j = \nabla_{\vec{X}}\xi_j/|\nabla_{\vec{X}}\xi_j| = \left(n_j^{(1)}, n_j^{(2)}\right)$ be the unit normal vector to the ξ_j-direction, and let $\vec{t}_j = \left(t_j^{(1)}, t_j^{(2)}\right) = \left(-n_j^{(2)}, n_j^{(1)}\right)$ be the respective unit transverse vector. Then the velocity vector $\vec{u}$ in the Cartesian coordinate can be projected into the local $\vec{n}_j$ and $\vec{t}_j$ coordinate as $\vec{u} = \upsilon_j\vec{n}_j + \omega_j\vec{t}_j$, where $\upsilon_j = \vec{u}\cdot\vec{n}_j$ is the component in the $\vec{n}_j$-direction and $\omega_j = \vec{u}\cdot\vec{t}_j$ is the component in the $\vec{t}_j$-direction.

With these definitions, the eigenvalues λ_j of matrix A_j for $j = 1, 2$ can be computed in a standard way (cf. [52]), and the results for the general moving grid case, $h \neq 0$, are

$$
\begin{array}{ll}
\lambda_{j,0} = 0 & \text{(algebraic multiplicity 4)}, \\
\lambda_{j,1} = U_j - c\left|\nabla_{\vec{X}}\xi_j\right| & \text{(algebraic multiplicity 1)}, \\
\lambda_{j,2} = U_j & \text{(algebraic multiplicity 4)}, \\
\lambda_{j,3} = U_j + c\left|\nabla_{\vec{X}}\xi_j\right| & \text{(algebraic multiplicity 1)},
\end{array}
\tag{19}
$$

where $c = \sqrt{\gamma(p+p_0)/\rho}$ is the speed of sound of the fluid. Note that in this work we assume that the thermodynamic description of the materials of interest is limited by the stability requirement that the speed of sound c belongs to a set of real numbers, and so all the eigenvalues λ_j that appear in (19) are real for $j = 1, 2$.

In the current instance, with the help of a symbolic algebra software such as Maple, the corresponding right eigenvectors for matrix A_1 are: for $\lambda_{1,1}$,

$$r_{1,1} = \left[1,\ u_1 - n_1^{(1)}c_1^{(-)},\ u_2 - n_1^{(2)}c_1^{(-)},\ H - \upsilon_1 c_1^{(-)} - \frac{ph\beta_1^{(-)}}{\rho},\ \frac{\mathcal{B}}{\Gamma},\ 0,\ \frac{hn_1^{(1)}c_1^{(-)}}{\rho J\lambda_{1,1}},\ \frac{hn_1^{(2)}c_1^{(-)}}{\rho J\lambda_{1,1}},\ 0,\ 0\right]^T,$$

for $\lambda_{1,2}$,

$$\begin{aligned}
r_{1,2} &= \left[1,\ u_1,\ u_2,\ \frac{K}{\Gamma},\ 0,\ 0,\ 0,\ 0,\ 0,\ 0\right]^T,\\
r_{1,3} &= \left[0,\ U_1 t_1^{(1)},\ U_1 t_1^{(2)},\ \omega_1 U_1,\ 0,\ 0,\ \frac{hn_1^{(2)}}{\rho J},\ -\frac{hn_1^{(1)}}{\rho J},\ 0,\ 0\right]^T,\\
r_{1,4} &= [0,\ 0,\ 0,\ -1,\ 1,\ 0,\ 0,\ 0,\ 0,\ 0]^T,\\
r_{1,5} &= \left[0,\ 0,\ 0,\ \frac{\varphi J}{\Gamma},\ 0,\ 1,\ 0\ ,0,\ 0,\ 0\right]^T,
\end{aligned}$$

for $\lambda_{1,3}$,

$$r_{1,6} = \left[1,\ u_1 + n_1^{(1)}c_1^{(+)},\ u_2 + n_1^{(2)}c_1^{(+)},\ H + \upsilon_1 c_1^{(+)} + \frac{ph\beta_1^{(+)}}{\rho},\ \frac{\mathcal{B}}{\Gamma},\ 0,\ -\frac{hn_1^{(1)}c_1^{(+)}}{\rho J\lambda_{1,3}},\ -\frac{hn_1^{(2)}c_1^{(+)}}{\rho J\lambda_{1,3}},\ 0,\ 0\right]^T,$$

and for $\lambda_{1,0}$,

$$\begin{aligned}
r_{1,7} &= [0,\ 0,\ 0,\ 0,\ 0,\ 0,\ \chi_{21},\ \chi_{22},\ 0,\ 0]^T,\\
r_{1,8} &= \left[1,\ u_1,\ u_2,\ \frac{E}{\rho},\ 0,\ 0,\ \frac{\chi_{11}}{\rho J},\ \frac{\chi_{12}}{\rho J},\ 0,\ 0\right]^T.
\end{aligned}$$

Moreover, the right eigenvectors for matrix A_2 are: for $\lambda_{2,1}$,

$$r_{2,1} = \left[1,\ u_1 - n_2^{(1)}c_2^{(-)},\ u_2 - n_2^{(2)}c_2^{(-)},\ H - \upsilon_2 c_2^{(-)} - \frac{ph\beta_2^{(-)}}{\rho},\ \frac{\mathcal{B}}{\Gamma},\ 0,\ 0,\ 0,\ \frac{hn_2^{(1)}c_2^{(-)}}{\rho J\lambda_{2,1}},\ \frac{hn_2^{(2)}c_2^{(-)}}{\rho J\lambda_{2,1}}\right]^T,$$

for $\lambda_{2,2}$,

$$\begin{aligned}
r_{2,2} &= \left[1,\ u_1,\ u_2,\ \frac{K}{\Gamma},\ 0,\ 0,\ 0,\ 0,\ 0,\ 0\right]^T,\\
r_{2,3} &= \left[0,\ U_2 t_2^{(1)},\ U_2 t_2^{(2)},\ \omega_2 U_2,\ 0,\ 0,\ 0,\ 0,\ \frac{hn_2^{(2)}}{\rho J},\ -\frac{hn_2^{(1)}}{\rho J}\right]^T,\\
r_{2,4} &= [0,\ 0,\ 0,\ -1,\ 1,\ 0,\ 0,\ 0,\ 0,\ 0]^T,\\
r_{2,5} &= \left[0,\ 0,\ 0,\ \frac{\varphi J}{\Gamma},\ 0,\ 1,\ 0\ ,0,\ 0,\ 0\right]^T,
\end{aligned}$$

for $\lambda_{2,3}$,

$$r_{2,6} = \left[1,\ u_1 + n_2^{(1)}c_2^{(+)},\ u_2 + n_2^{(2)}c_2^{(+)},\ H + \upsilon_2 c_2^{(+)} + \frac{ph\beta_2^{(+)}}{\rho},\ \frac{\mathcal{B}}{\Gamma},\ 0,\ 0,\ 0,\ -\frac{hn_2^{(1)}c_2^{(+)}}{\rho J\lambda_{2,3}},\ -\frac{hn_2^{(2)}c_2^{(+)}}{\rho J\lambda_{2,3}}\right]^T,$$

and for $\lambda_{2,0}$,

$$r_{2,7} = [0,\ 0,\ 0,\ 0,\ 0,\ 0,\ 0,\ 0,\ \chi_{11},\ \chi_{12}]^T,$$
$$r_{2,8} = \left[1,\ u_1,\ u_2,\ \frac{E}{\rho},\ 0,\ 0,\ 0,\ 0,\ \frac{\chi_{21}}{\rho J},\ \frac{\chi_{22}}{\rho J}\right]^T.$$

Here we have $c_j^{(\pm)} = c(1 \pm h\beta_j^{(\pm)})$, $\beta_j^{(-)} = c|\nabla_{\vec{X}}\xi_j|/(\lambda_{j,1} + ch|\nabla_{\vec{X}}\xi_j|)$, and $\beta_j^{(+)} = c|\nabla_{\vec{X}}\xi_j|/(\lambda_{j,3} - ch|\nabla_{\vec{X}}\xi_j|)$ for $j = 1, 2$.

From the above, it is easy to observe that in either case the geometric multiplicity of the zero eigenvalue $\lambda_{1,0}$ or $\lambda_{2,0}$ is 2, but is not 4, yielding two missing eigenvectors for matrices A_1 and A_2 (this is not surprising however because there are two null vectors in each of these matrices). In addition, in case the contravariant velocity U_j in the ξ_j-direction is happened to be zero which would occur in particular when $h = 1$ or $\vec{u} = 0$ as seen from (15), we loss another eigenvector for matrix A_j because the two previously linearly independent eigenvectors $r_{j,3}$ and $r_{j,7}$ becomes parallel to each other. In view of this fact that, we conclude that our two-fluid model in the generalized Lagrangian coordinate (13) is only weakly hyperbolic in two dimensions; this can be shown to be true in any N_d space dimension, with the exception of $N_d = 1$ (cf. [16, 17]). A more detailed discussion about the mathematical significance of the loss of strong hyperbolicity for the Lagrangian gas dynamics system in two dimensions is given in [9], for example. Surely, in the Eulerian case, $h = 0$, where the basic motion of the flow is governed by (11), our model system can be shown to be of (strongly) hyperbolic type that satisfies all the requirement mentioned above, irrespective of the number of space dimension.

4 Wave propagation methods

To find approximate solutions of our homogeneous two-fluid flow model (13) in a generalized coordinate that contains spatially varying metrics in the flux functions of the physical conservation laws, we use a flux-based wave decomposition method developed by Bale *et al.* [2, 40] with the dimensional-splitting technique incorporated in the method for multidimensional problems. This method is a variant of the standard wave-propagation scheme [26, 48] in that we solve one-dimensional Riemann problems at each cell interface as usual, but rather than using the resulting jumps of the state variables moving at constant speeds to update the solutions in neighboring grid cells, we use the resulting jumps of fluxes for that instead, which has shown (cf. [2]) to be a much more accurate approach than the former one for a class of hyperbolic problems with spatially varying fluxes (this is the type of problems concerned here).

To explain the basic idea of the method, we consider the two-dimensional case $N_d = 2$ as an example, and so in a simple dimensional-splitting approach the equations to be solved

$$\frac{\partial q}{\partial \tau} + f_1\left(\frac{\partial}{\partial \xi_1}, q\right) + f_2\left(\frac{\partial}{\partial \xi_2}, q\right) = 0$$

with q, f_1 and f_2 defined by (14a), (14b), and (14c), respectively, are split into a sequence of one-dimensional problems as

$$\xi_1\text{-sweeps:} \qquad \frac{\partial q}{\partial \tau} + f_1\left(\frac{\partial}{\partial \xi_1}, q\right) = 0, \tag{20a}$$
$$\xi_2\text{-sweeps:} \qquad \frac{\partial q}{\partial \tau} + f_2\left(\frac{\partial}{\partial \xi_2}, q\right) = 0. \tag{20b}$$

Assuming a uniform rectangular grid with a fixed mesh spacing $\Delta\xi_1$ in the ξ_1-direction and $\Delta\xi_2$ in the ξ_2-direction that discretizes a logical domain as illustrated in Fig. 2, for instance. The method uses a

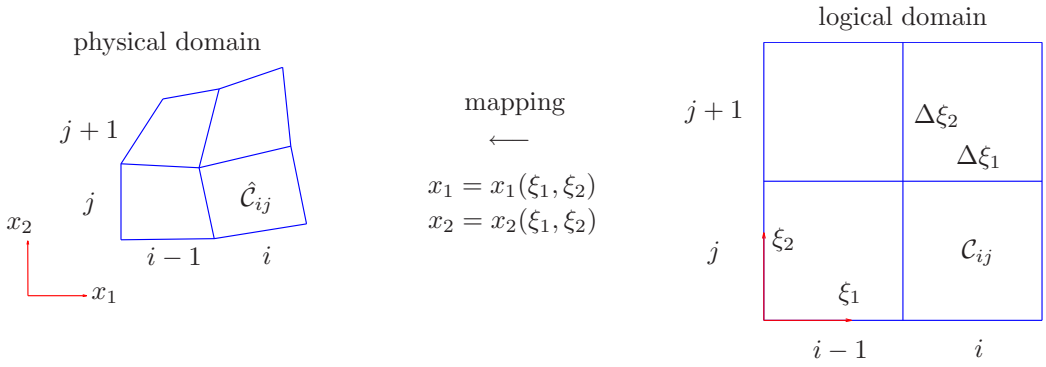

Figure 2: A sample grid system that is formed at a time in our two-dimensional generalized Lagrangian scheme. The numerical solution on the rectangular grid cell $\mathcal{C}_{ij}$ in the logical domain gives distinctively the result on the mapped quadrilateral grid cell $\hat{\mathcal{C}}_{ij}$ in the physical domain for all the grid cell (i, j).

standard finite-volume formulation in which the approximate value Q_{ij}^n of the cell average of the solution over the (i, j)th grid cell at time τ_n can be written as

$$Q_{ij}^n \approx \frac{1}{\Delta\xi_1 \Delta\xi_2} \int_{\mathcal{C}_{ij}} q(\xi_1, \xi_2, \tau_n)\, d\xi_1\, d\xi_2,$$

where $\mathcal{C}_{ij}$ denotes the rectangular region occupied by the grid cell (i, j). Note that in the algorithm the numerical solution on the rectangular grid cell $\mathcal{C}_{ij}$ in the logical domain gives distinctively the result on the mapped quadrilateral grid cell $\hat{\mathcal{C}}_{ij}$ in the physical domain for all the grid cell (i, j), see Fig. 2. The time step from the current time τ_n to the next τ_{n+1} is denoted by $\Delta\tau$.

In this numerical setup, a dimensional-splitting (or called Godunov-splitting) version of the first-order wave-propagation method in two dimensions can be written as

$$Q_{ij}^* = Q_{ij}^n - \frac{\Delta\tau}{\Delta\xi_1} \left[\left(\mathcal{A}_1^+ \Delta Q\right)_{i-1/2,j}^n + \left(\mathcal{A}_1^- \Delta Q\right)_{i+1/2,j}^n \right], \tag{21a}$$

$$Q_{ij}^{n+1} = Q_{ij}^* - \frac{\Delta\tau}{\Delta\xi_2} \left[\left(\mathcal{A}_2^+ \Delta Q\right)_{i,j-1/2}^* + \left(\mathcal{A}_2^- \Delta Q\right)_{i,j+1/2}^* \right]. \tag{21b}$$

Here in the ξ_1-sweeps we start with cell average Q_{ij}^n at time τ_n and solve (20a) along each row of cells $\mathcal{C}_{ij}$ with j fixed, updating Q_{ij}^n to Q_{ij}^* by the use of (21a) with the fluctuations

$$\left(\mathcal{A}_1^+ \Delta Q\right)_{i-1/2,j}^n = \sum_{m:(\lambda_{1,m})_{i-1/2,j}^n > 0} \left(\mathcal{Z}_{1,m}\right)_{i-1/2,j}^n$$

and

$$\left(\mathcal{A}_1^- \Delta Q\right)_{i+1/2,j}^n = \sum_{m:(\lambda_{1,m})_{i+1/2,j}^n < 0} \left(\mathcal{Z}_{1,m}\right)_{i+1/2,j}^n,$$

where $(\lambda_{1,m})_{\iota-1/2,j}^n$ and $(\mathcal{Z}_{1,m})_{\iota-1/2,j}^n$ are in turn the wave speed and the f-waves (the flux-based wave decomposition) for the mth family of the solutions obtained from solving the one-dimensional Riemann problems in the direction normal to the cell interface between $\mathcal{C}_{\iota-1,j}$ and $\mathcal{C}_{\iota j}$ with $Q_{\iota-1,j}^n$ and $Q_{\iota j}^n$ as initial data, see Section 5 for the details. Then in the ξ_2-sweeps we can use the Q_{ij}^* values as data for solving (20b) along each column of cells $\mathcal{C}_{ij}$ with i fixed, which gives us the solution of the next time step Q_{ij}^{n+1} from (21b) with the fluctuations

$$\left(\mathcal{A}_2^+ \Delta Q\right)_{i,j-1/2}^* = \sum_{m:(\lambda_{2,m})_{i,j-1/2}^* > 0} \left(\mathcal{Z}_{2,m}\right)_{i,j-1/2}^*$$

and

$$(\mathcal{A}_2^- \Delta Q)^*_{i,j+1/2} = \sum_{m:(\lambda_{2,m})^*_{i,j+1/2}<0} (\mathcal{Z}_{2,m})^*_{i,j+1/2}\,.$$

It is clear that this method belongs to a class of upwind schemes, and is stable when the typical CFL (Courant-Friedrichs-Lewy) condition:

$$\nu = \frac{\Delta\tau \max_m (\lambda_{1,m}, \lambda_{2,m})}{\min(\Delta\xi_1, \Delta\xi_2)} \le 1, \tag{22}$$

is satisfied (cf. [11, 25, 26]). Moreover, it is not difficult to show that the method is quasi-conservative in the sense that when applying the method to (13) not only the conservation laws but also the transport equations are approximated in a consistent manner by the method.

To extend this splitting method to a high-resolution version (*i.e.*, second-order accurate on smooth solutions, and sharp and monotone profiles on discontinuous solutions), it is a common practice to modify (21a) and (21b), in a respective manner, as

$$Q^*_{ij} = Q^n_{ij} - \frac{\Delta\tau}{\Delta\xi_1}\left[(\mathcal{A}_1^+\Delta Q)^n_{i-1/2,j} + (\mathcal{A}_1^-\Delta Q)^n_{i+1/2,j}\right] - \frac{\Delta\tau}{\Delta\xi_1}\left[\left(\tilde{\mathcal{F}}_1\right)^n_{i+1/2,j} - \left(\tilde{\mathcal{F}}_1\right)^n_{i-1/2,j}\right]$$

and

$$Q^{n+1}_{ij} = Q^*_{ij} - \frac{\Delta\tau}{\Delta\xi_2}\left[(\mathcal{A}_2^+\Delta Q)^*_{i,j-1/2} + (\mathcal{A}_2^-\Delta Q)^*_{i,j+1/2}\right] - \frac{\Delta\tau}{\Delta\xi_2}\left[\left(\tilde{\mathcal{F}}_2\right)^*_{i,j+1/2} - \left(\tilde{\mathcal{F}}_2\right)^*_{i,j-1/2}\right],$$

where the add in correction terms such as $(\tilde{\mathcal{F}}_1)^n_{i-1/2,j}$ and $(\tilde{\mathcal{F}}_2)^*_{i,j-1/2}$, for example, written in view of the f-waves approach with m_w wave family in total may have the form

$$(\tilde{\mathcal{F}}_1)^n_{i-1/2,j} = \frac{1}{2}\sum_{m=1}^{m_w}\left[\mathrm{sign}(\lambda_{1,m})\left(1 - \frac{\Delta\tau}{\Delta\xi_1}|\lambda_{1,m}|\right)\tilde{\mathcal{Z}}_{1,m}\right]^n_{i-1/2,j}$$

and

$$(\tilde{\mathcal{F}}_2)^*_{i,j-1/2} = \frac{1}{2}\sum_{m=1}^{m_w}\left[\mathrm{sign}(\lambda_{2,m})\left(1 - \frac{\Delta\tau}{\Delta\xi_2}|\lambda_{2,m}|\right)\tilde{\mathcal{Z}}_{2,m}\right]^*_{i,j-1/2},$$

see [2, 26] for more expositions. Note that $\tilde{\mathcal{Z}}_{\iota,m}$ is a limited value of $\mathcal{Z}_{\iota,m}$ obtained by comparing $\mathcal{Z}_{\iota,m}$ with the corresponding $\mathcal{Z}_{\iota,m}$ from the neighboring Riemann problem to the left (if $\lambda_{\iota,m} > 0$) or to the right (if $\lambda_{\iota,m} < 0$) for $\iota = 1, 2$.

To end this section, we want to mention that the extension of this wave propagation method from two to three space dimensions can be done in a straightforward manner when the solutions of one-dimensional Riemann problems in each dimensional-sweep can be computed readily (cf. [17]).

5 Riemann problem and approximate solutions

To determine the aforementioned wave speeds and fluctuations in the wave-propagation methods, we need to solve one-dimensional Riemann problems in direction normal to each cell interfaces. If we consider the case between cells $\mathcal{C}_{i-1,j}$ and $\mathcal{C}_{ij}$ as illustrated in Fig. 2, for example, it would be a standard one when we define the normal Riemann problem to this face as a Cauchy problem that consists of the equations (20a) with the piecewise constant initial data

$$q(\xi_1, 0) = \begin{cases} Q^n_{i-1,j} & \text{if } \xi_1 < (\xi_1)_{i-1/2}, \\ Q^n_{ij} & \text{if } \xi_1 > (\xi_1)_{i-1/2}. \end{cases} \tag{23}$$

In this instance, from (20a) it is easy to observe that all the flux functions for the conservation laws,*i.e.*, $\breve{f}_1$ given in (17a), of the Riemann problem bears some relations to the time-independent part of the geometric variables $\chi_{21} = \partial_{\xi_2} x_1$ and $\chi_{22} = \partial_{\xi_2} x_2$, while there is no relation for any of them to the remaining time-dependent geometric variables $\chi_{11} = \partial_{\xi_1} x_1$ and $\chi_{12} = \partial_{\xi_1} x_2$. With this in mind, it should be sensible (cf. [2, 17, 18, 19, 36, 37]) to put the original Riemann problem into a new generalized form as

$$\begin{cases} \dfrac{\partial q_{i-1,j}}{\partial \tau} + f_1\left(\dfrac{\partial}{\partial \xi_1}, q_{i-1,j}\right) = 0 & \text{if } \xi_1 < (\xi_1)_{i-1/2}, \\ \dfrac{\partial q_{ij}}{\partial \tau} + f_1\left(\dfrac{\partial}{\partial \xi_1}, q_{ij}\right) = 0 & \text{if } \xi_1 > (\xi_1)_{i-1/2}, \end{cases} \tag{24}$$

for the equations and (23) for the initial data as before. Here in the above we have used a cell-average approach where q and $f_1(\partial_{\xi_1}, q)$ are discretized to yield a new function $q_{ij} = q|_{(\chi_{21},\chi_{22})_{ij}}$ and $f_1(\partial_{\xi_1}, q_{ij}) = f_1(\partial_{\xi_1}, q)|_{(\chi_{21},\chi_{22})_{ij}}$, respectively, that holds throughout the grid cell $\mathcal{C}_{ij}$.

We note that as to the normal-direction $(\vec{n}_1)_{i-1/2,j} = (\nabla_{\vec{X}}\xi_1/|\nabla_{\vec{X}}\xi_1|)_{i-1/2,j}$ to the cell interface $(\xi_1)_{i-1/2}$ which should be a constant vector with unit length in this Riemann problem, we use the relation

$$(\vec{n}_1)_{i-1/2,j} = (\bar{\chi}_{22}, -\bar{\chi}_{21})/\bar{S} \tag{25}$$

for that, where $\bar{z} = (z_{i-1,j} + z_{ij})/2$ is the average value of $z_{i-1,j}$ and z_{ij} for $z = \chi_{21}$, χ_{22}, and $\bar{S} = \sqrt{\bar{\chi}_{21}^2 + \bar{\chi}_{22}^2}$ is the Euclidean distance of the vector $(\bar{\chi}_{22}, -\bar{\chi}_{21})$ in two dimensions. With that, the transverse-direction to this cell interface is taken to be $(\vec{t}_1)_{i-1/2,j} = (\bar{\chi}_{21}, \bar{\chi}_{22})/\bar{S}$.

Recall that, for the single component case with the ideal gas law, it has been demonstrated by Hui and coworkers [17, 19] that with a reasonable set of the initial data solutions of this generalized Riemann problem exist that consist of the classical self-similar solutions such as shock waves, rarefaction waves, and contact discontinuities, for gas dynamics, and an additional stationary discontinuity at the cell interface (to be called a cell-edge discontinuity below) where there are only jumps on the geometric variables but are uniform on the physical flow variables across it, see Fig. 3 for an illustration of the basic solution structure. As a consequence, in their work, they are able to take the usual procedures as if there is no such a cell-edge discontinuity to the construction of the exact solution for the Riemann problem, see [18] also for more discussion when the shallow water equations are involved in the problem formulation.

Due to the possible loss of strong hyperbolicity of the proposed model, see Section 3, which would lead to numerical difficulties in using a linearized Riemann solver based on eigenvector decomposition of state variables (cf. [38, 55]), in the current work with the homogeneous two-fluid model (13) and the stiffened gas equation of state (2), we are interested in a popular shock-only (or called two-shock) approach (cf. [6]) that ignores the possibility of rarefaction waves and simply build a solution in which each pair of the states is connected along the Hugoniot locus for a shock. To simplify the notation in the following discussion, we denote $z_L = z_{i-1,j}^n$ and $z_R = z_{ij}^n$ as being the Riemann data for a state variable z on the left and right of the cell interface, respectively. We then write the rotated velocity components of the Riemann data in the normal- and transverse-direction to the cell interface as $\upsilon_\iota = \vec{u}_\iota \cdot (\vec{n}_1)_{i-1/2,j}$ and $\omega_\iota = \vec{u}_\iota \cdot (\vec{t}_1)_{i-1/2,j}$, in an respective manner, for $\iota = L$ or R.

As in the standard Riemann problem on general quadrilateral grids (cf. [3, 26]), the key step in this shock-only approach is to find the midstate (υ_m, p_m) in the υ-p phase plane so that it can connect to (υ_L, p_L) by a 1-shock, and to (υ_R, p_R) by a 3-shock. For that, this amounts to solving the following nonlinear equation in an iterative manner for the pressure p_m:

$$\psi(p_m) = \upsilon_{mR}(p_m) - \upsilon_{mL}(p_m) = 0. \tag{26}$$

Here υ_{mL} and υ_{mR} are the velocities defined by connecting the states along the 1-shock and 3-shock

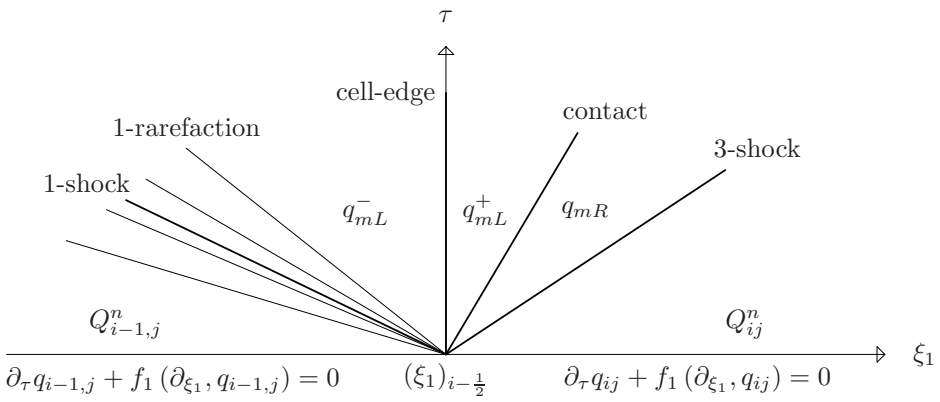

Figure 3: Typical solution structure of the generalized Riemann problem for our homogeneous two-fluid model discussed in Section 5. The key step in obtaining this solution is to find the pressure and the velocity (the normal component of it) in the regions m_L and m_R where both of them are continuous across the contact and the cell-edge discontinuities. Note that there are only jumps in the geometric variables across the cell-edge discontinuity that separates the constant states q^-_{mL} and q^+_{mL}. In a shock-only approximate Riemann solver, the rarefaction wave is replaced by an entropy-violating shock.

curves, respectively,

$$\upsilon_{mL}(p) = \upsilon_L - \frac{p - p_L}{M_L(p)}, \qquad \upsilon_{mR}(p) = \upsilon_R + \frac{p - p_R}{M_R(p)}, \tag{27}$$

with M_ι denoting the Lagrangian shock speed, for $\iota = L$ or R. In the current application of the pressure law (2), we may compute M_ι quite easily by evaluating the formula

$$M^2_\iota(p) = C^2_\iota \left[1 + \left(\frac{\gamma_\iota + 1}{2\gamma_\iota}\right)\left(\frac{p + p_{0\iota}}{p_\iota + p_{0\iota}} - 1\right)\right] \tag{28}$$

where $C_\iota = \rho_\iota c_\iota$ is the Lagrangian sound speed, and $\rho_{m\iota}$ is the midstate density on the ι side,

$$\rho_{m\iota}(p) = \left[\rho_\iota^{-1} - \frac{p - p_\iota}{M^2_\iota(p)}\right]^{-1} \tag{29}$$

Note that (28) and (29) are as a result derived from the Rankine-Hugoniot jump conditions across the shock waves (cf. [8, 17, 19]).

When applying a standard root-finding approach such as the secant method to (26), we have a 2-step iteration scheme as follows,

$$p^{(k+1)}_m = p^{(k)}_m - \frac{\left|p^{(k)}_m - p^{(k-1)}_m\right|}{\left|\upsilon^{(k)}_{mL} - \upsilon^{(k-1)}_{mL}\right| + \left|\upsilon^{(k)}_{mR} - \upsilon^{(k-1)}_{mR}\right|}\left[\upsilon^{(k)}_{mR} - \upsilon^{(k)}_{mL}\right], \tag{30}$$

where $\upsilon^{(k)}_{m\iota} = \upsilon_{m\iota}\left[p^{(k)}_m\right]$, for $\iota = L$ or R, and $k = 1, 2, \ldots$ (until convergence). With a suitable choice of the starting values $p^{(0)}_m$ and $p^{(1)}_m$, method (30) typically converges to the exact solution p_m at a super linear rate [22]. For gas dynamics, it is a common practice to set $p^{(0)}_m$ and $p^{(1)}_m$ by

$$\begin{aligned} p^{(0)}_m &= \frac{p_R C_L + p_L C_R - (\upsilon_R - \upsilon_L) C_L C_R}{C_L + C_R}, \\ p^{(1)}_m &= \frac{p_R M^{(0)}_L + p_L M^{(0)}_R - (\upsilon_R - \upsilon_L) M^{(0)}_L M^{(0)}_R}{M^{(0)}_L + M^{(0)}_R}, \end{aligned} \tag{31}$$

where $M_\iota^{(0)} = M_\iota\left[p_m^{(0)}\right]$. Having that, we may assign $\upsilon_{mL}^{(0)}$ and $\upsilon_{mR}^{(0)}$ by

$$\upsilon_{mL}^{(0)} = \upsilon_L - \frac{p_m^{(0)} - p_L}{C_L}, \qquad \upsilon_{mR}^{(0)} = \upsilon_R + \frac{p_m^{(0)} - p_R}{C_R},$$

and $\upsilon_{mL}^{(1)}$ and $\upsilon_{mR}^{(1)}$ according to (27). After a satisfactory convergence of the scheme, υ_m can then be calculated based on the formula:

$$\upsilon_m = \frac{p_L - p_R + \upsilon_L M_L(p_m) + \upsilon_R M_R(p_m)}{M_L(p_m) + M_R(p_m)}.$$

Figure 3 illustrates a typical solution structure of the present two-fluid generalized Riemann problem. Clearly, in a two-shock approximate solver, we replace the leftward-going 1-rarefaction wave by a 1-shock, and so the solution would consist of four discontinuities moving at constant speeds. Here the propagation speed of each discontinuity is determined by

$$\begin{aligned}
(\lambda_{1,0})_{i-1/2,j} &= 0, \\
(\lambda_{1,1})_{i-1/2,j} &= \left[(1-h)\upsilon_m - \frac{M_L(p_m)}{\rho_{mL}(p_m)}\right]\left|\nabla_{\vec{X}}\xi_1\right|_{i-1/2,j}, \\
(\lambda_{1,2})_{i-1/2,j} &= (1-h)\upsilon_m\left|\nabla_{\vec{X}}\xi_1\right|_{i-1/2,j}, \\
(\lambda_{1,3})_{i-1/2,j} &= \left[(1-h)\upsilon_m + \frac{M_R(p_m)}{\rho_{mR}(p_m)}\right]\left|\nabla_{\vec{X}}\xi_1\right|_{i-1/2,j},
\end{aligned} \tag{32}$$

where $\left|\nabla_{\vec{X}}\xi_1\right|_{i-1/2,j}$ is a scale factor for the wave speed which can be taken as an average value based on $\left|\nabla_{\vec{X}}\xi_1\right|_L$ and $\left|\nabla_{\vec{X}}\xi_1\right|_R$, for example. We note that the zero th- and the second-wave families, *i.e.*, the case with speeds $\lambda_{1,0}$ and $\lambda_{1,2}$, respectively, would correspond to the linearly degenerate field such as the cell-edge and contact discontinuities, and the remaining wave families, *i.e.*, the case with speeds $\lambda_{1,1}$ and $\lambda_{1,3}$, would correspond to the genuinely nonlinear field such as the shock waves and rarefactions (cf. [51]).

To define the jumps across each of these discontinuities, in a spatially varying fluxes case as the one considered here, it is known (cf. [2, 40]) to have the advantage of using a variant of the flux-based wave decomposition approach in that the flux difference $\breve{f}_1(Q_R) - \breve{f}_1(Q_L)$ (see (17a) for the definition of $\breve{f}_1$) is decomposed into a sum of the difference between the fluxes to the left and right of the discontinuity,

$$\breve{f}_1(Q_R) - \breve{f}_1(Q_L) = \sum_{m=0}^{3} (\mathcal{Z}_{1,m})_{i-1/2,j},$$

where in the wave configuration shown in Fig. 3, for example, we have

$$\begin{aligned}
(\mathcal{Z}_{1,0})_{i-1/2,j} &= \breve{f}_1\left(q_{mL}^+\right) - \breve{f}_1\left(q_{mL}^-\right), \\
(\mathcal{Z}_{1,1})_{i-1/2,j} &= \breve{f}_1\left(q_{mL}^-\right) - \breve{f}_1\left(Q_L\right), \\
(\mathcal{Z}_{1,2})_{i-1/2,j} &= \breve{f}_1\left(q_{mR}\right) - \breve{f}_1\left(q_{mL}^+\right), \\
(\mathcal{Z}_{1,3})_{i-1/2,j} &= \breve{f}_1\left(Q_R\right) - \breve{f}_1\left(q_{mR}\right),
\end{aligned} \tag{33}$$

with a modification on the sixth-component of the second-wave family (*i.e.*, for the contact discontinuity) as

$$\left(\mathcal{Z}_{1,2}^{(6)}\right)_{i-1/2,j} = (\lambda_{1,2})_{i-1/2,j}(\alpha_R - \alpha_L)$$

that takes account of the effect due to the non-conservative transport equation for the volume fraction when $h \neq 1$. Note that in (33) $\breve{f}_1\left(q_{mL}^-\right)$ is calculated using the data: ρ_{mL}, υ_m, ω_L, p_m, γ_L, $\mathcal{B}_L$, p_{0L},

$(\chi_{21})_L$, $(\chi_{22})_L$, $\breve{f}_1\left(q^+_{mL}\right)$ is calculated using the data: ρ_{mL}, υ_m, ω_L, p_m, γ_L, $\mathcal{B}_L$, p_{0L}, $(\chi_{21})_R$, $(\chi_{22})_R$, and $\breve{f}_1\left(q_{mR}\right)$ is calculated using the data: ρ_{mR}, υ_m, ω_R, p_m, γ_R, $\mathcal{B}_R$, p_{0R}, $(\chi_{21})_R$, $(\chi_{22})_R$. As usual, wave propagation methods are based on using these propagating discontinuities to update the cell averages in the cells neighboring to each interface, see Section 4.

As a final remark, when a more general equation of state (cf. [7, 46]) is included in the problem formulation, due to the complexity that is involved to find the midstate (υ_m, p_m), this shock-only solver may not be an effective one to be used for the numerical resolution of the Riemann problem. The development of a simplier HLL-type (cf. [14, 55]) or Roe-type (cf. [36, 37, 38]) solver for the proposed generalized Riemann problem would become necessary; this is the subject to be discussed in a sequel paper elsewhere.

6 Numerical results

We now present some sample numerical results obtained using our algorithm described in Sections 4 and 5 for single- and two-component inviscid compressible flow problems in one and two space dimensions. Without stated otherwise, we have carried out all the tests using the Courant number $\nu = 0.5$ defined by (22), the grid-movement parameter $h = 0.99$, and the MINMOD limiter in the high-resolution version of the finite-volume method based on f-wave formulation. The material-dependent parameters in the stiffened gas equation of state (2) are set to be $(\gamma,\ \rho_0,\ \mathcal{B}) = (1.4,\ 1.2\text{kg/m}^3,\ 0)$ and $(4.4,\ 10^3\text{kg/m}^3,\ 2.64 \times 10^6(\text{m/s})^2)$ for the gas- and liquid-phase (*i.e.*, for the air and water), respectively. For comparison purposes, we have also included Eulerian results when $h = 0$ is employed in the method to the problems.

6.1 One-dimensional case

EXAMPLE 6.1.1. To begin with, we consider a two-component version of the Lax Riemann problem where a variant of this problem in the single component case is one of the popular tests for numerical validation of a Lagrangian-type scheme (cf. [9, 43]). Initially, on the left when $x_1 \in [0, 0.5)$, we have the perfect gas with the state variables

$$(\rho,\ u_1,\ p,\ \gamma,\ \mathcal{B},\ \alpha)_L = (0.445,\ 0.698,\ 3.528,\ 1.4,\ 0,\ 1)\,,$$

while on the right when $x_1 \in [0.5, 1]$, we have a different perfect gas with the state variables

$$(\rho,\ u_1,\ p,\ \gamma,\ \mathcal{B},\ \alpha)_R = (0.5,\ 0,\ 0.571,\ 1.2,\ 0,\ 0)\,.$$

The exact solution of this problem consists of a leftward-going rarefaction wave, a rightward-going contact discontinuity, and a shock wave.

Figure 4 shows numerical results for the density, velocity, and pressure at time $t = 0.14$ with a 100 mesh points. From the figure, it is easy to observe a sharper resolution of the contact discontinuity, when the density profile is in comparison with the one obtained using the Eulerian $h = 0$ version of the method. In addition, the shock and rarefaction waves are in good agreement with the exact solution as well. To demonstrate the time variation of the physical grid coordinates generated by our algorithm, in Fig. 5 we display a sample of them at eleven different times $t = i \times 0.014$, for $i = 0, 1, \ldots, 10$. The dynamic movement of the grid system is clearly seen. It should be noted that each little dashed lines displayed in that graph gives a cell-center location of the grid at a specific output time. Here the non-reflecting outflow boundaries are used on the left and right computational domain.

EXAMPLE 6.1.2. To see how our algorithm works for complex wave interactions, we are concerned with a model single-component (gas-phase only) problem studied by Woodward and Colella [56, 57]. In

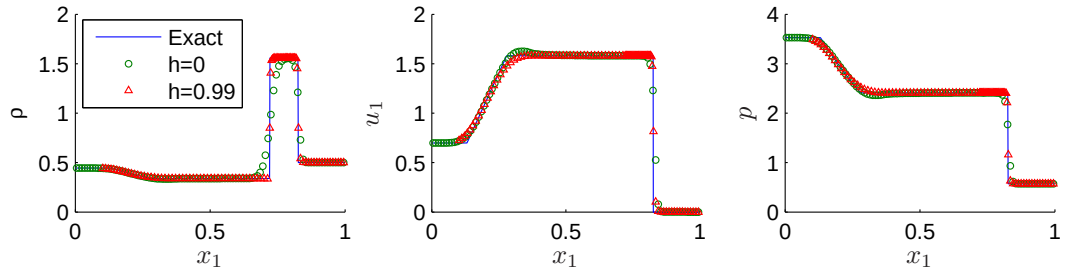

Figure 4: Numerical results for a two-component Lax Riemann problem at time $t = 0.14$. The solid line is the exact solution, and the dotted and triangular points are the computed solutions obtained using two different grid-movement parameters $h = 0$ and $h = 0.99$, respectively, with a 100 mesh points.

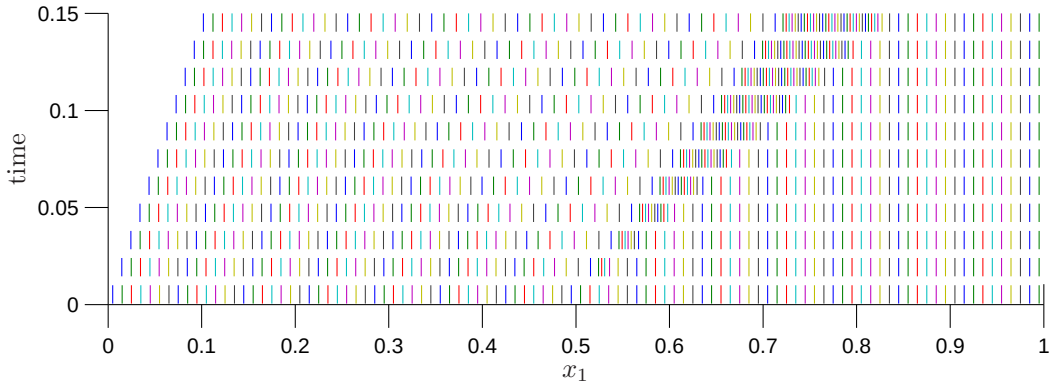

Figure 5: Physical grid coordinates for the generalized Lagrangian run shown in Fig. 4 at eleven different times $t = i \times 0.014$, for $i = 0, 1, \ldots, 10$. Each little dashed line displayed in the graph gives a cell-center location of the grid system at a specific output time.

this problem, the initial condition consists of three constant states with data

$$\begin{pmatrix} \rho \\ u_1 \\ p \end{pmatrix}_L = \begin{pmatrix} 1 \\ 0 \\ 10^3 \end{pmatrix}, \qquad \begin{pmatrix} \rho \\ u_1 \\ p \end{pmatrix}_M = \begin{pmatrix} 1 \\ 0 \\ 10^{-2} \end{pmatrix}, \qquad \begin{pmatrix} \rho \\ u_1 \\ p \end{pmatrix}_R = \begin{pmatrix} 1 \\ 0 \\ 10^2 \end{pmatrix},$$

where L is the state used for $x_1 \in [0, 0.1)$, M is the state used for $x_1 \in [0.1, 0.9)$, and R is the state used for $x_1 \in [0.9, 1]$. Here there are two solid walls at the left and right boundaries.

In this setup, it is known that, after breaking the membranes at $x = 0.1$ and 0.9, a shock wave, contact discontinuity, and rarefaction wave develop at each discontinuity individually. As time progresses, the shock waves move toward each other and then collide, yielding a new contact discontinuity from the collision. Further collisions then occur, see [27, 56] for a complete wave pattern of this problem in the space-time plane.

To solve this problem numerically, we use a 200 mesh points, and perform the computation in the same manner as in Example 6.1.1. In Fig. 6, the density, velocity, and pressure are presented at three different times $t = 0.016$, 0.032, and 0.038. From there, we again observe a sensible improvement of the contact discontinuities, especially, the emergent one after the head-on collision of the initial shock waves, when they are in comparison with the Eulerian results. Besides, we find good resolution of the

shock wave and rarefaction as we compare our numerical results with the fine grid solutions obtained using the Eulerian grid approach with a 2000 mesh points. The physical grid coordinates generated by our generalized Lagrangian algorithm are plotted in Fig. 7 at eleven different times $t = i \times 0.0038$, for $0, 1, \ldots, 10$, noticing interesting numerical temporal behavior of the grid movement that follows closely to the main feature of the underlying flow field.

6.2 Two-dimensional case

EXAMPLE 6.2.1. As a first example, we consider a single-component two-dimensional Riemann problem, *i.e.*, Configuration 4 studied by Schulz-Rinne *et al.* [42]. In this case, the initial condition is composed of four shock waves with the data in the four quadrants given by

$$(\rho,\ u_1,\ u_2,\ p)_1 = (1.1,\ 0,\ 0,\ 1.1)\,, \qquad (\rho,\ u_1,\ u_2,\ p)_2 = (0.5065,\ 0.8939,\ 0,\ 0.35)\,,$$
$$(\rho,\ u_1,\ u_2,\ p)_3 = (1.1,\ 0.8939,\ 0.8939,\ 1.1)\,, \quad (\rho,\ u_1,\ u_2,\ p)_4 = (0.5065,\ 0,\ 0.8939,\ 0.35)\,.$$

Here, the fluid component is a perfect gas throughout the whole unit square domain, and the boundary conditions are non-reflecting on all sides. Note that this problem has been used as a benchmark test to verify a cell-by-cell adaptive mesh Lagrangian scheme proposed by Morrell [35].

Numerical results for a sample run of this problem with two different grid-movement parameters $h = 0$ and 0.99 are shown in Fig. 8, where contour plots of the density and pressure, and the physical grid system are presented at time $t = 0.2$ with a 200×200 grid. From the figure, it is interesting to see that the collisions between the initial shock waves creates an oval shape region bounded by the incident and reflected shock waves. When we make a comparison of our results with the one appeared in Fig. 6 of [42], for instance, (which was done using a state-of-the-art second order Eulerian method with a 400×400 grids), we find notably a better resolution of our generalized result than the Eulerian one for the slip lines that are situated in the shock-waves bounded oval region, and similar solution behaviors for the location and structure of the reflected shock waves. To give a quantitative assessment of these solutions, Fig. 9 plots the cross section of the results for the same run along the diagonal axis of the computational grid, observing good agreement of the density and pressure profiles in most places, and some deviation in the density near the center of the oval region where the slip lines from the upper-left and lower-right corners collide with each other. We note that at those points of discrepancy the topology of the physical grid cells in the generalized Lagrangian case differ a lot from the Eulerian case, see Fig. 8, and so the finite-volume cell averages displayed there do not give exactly the same point-wise physical-state correspondence. Recall that J is the Jacobian of the grid metrics.

EXAMPLE 6.2.2. We are next concerned with a two-component (gas-liquid) radially symmetric problem that the computed solution in two dimensions can be compared to the one-dimensional results for numerical validation. We use the following set of data for experiments in which, inside a circle of radius $r_0 = 0.2$m, the fluid is a gas-phase with

$$(\rho,\ u_1,\ u_2\ ,\ p,\ \alpha)_{r \le r_0} = \left(1250\ \mathrm{kg/m^3},\ 0,\ 0,\ 10^9\ \mathrm{Pa},\ 1\right),$$

while outside the circle, the fluid is a liquid-phase with

$$(\rho,\ u_1,\ u_2,\ p,\ \alpha)_{r > r_0} = \left(10^3\ \mathrm{kg/m^3},\ 0,\ 0,\ 10^5\ \mathrm{Pa},\ 0\right),$$

where $r = \sqrt{(x_1 - x_1^0)^2 + (x_2 - x_2^0)^2}$ and $(x_1^0, x_2^0) = (0, 0)$. We note that due to the pressure difference between the fluids at $r = r_0$, breaking of the membrane occurs instantaneously, yielding an outward-going shock wave in liquid, an inward-going rarefaction wave in gas, and a outward-going contact discontinuity lying in between that separates the gas and liquid. We note that because of the symmetry of the solution,

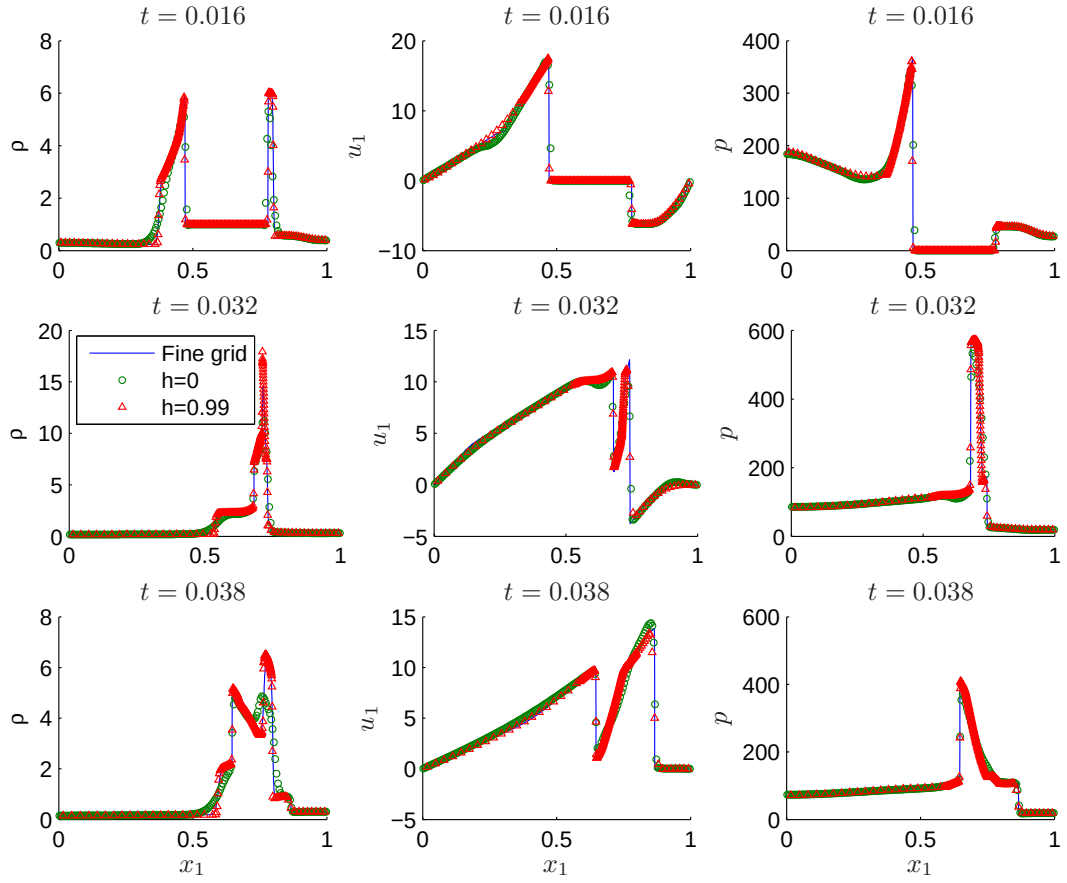

Figure 6: Numerical results for the Woodward-Colella problem at three different times $t = 0.016$, 0.032, and 0.038. Here the solid line is the fine grid solution obtained using the Eulerian grid approach with a 2000 mesh points, and the dotted and triangular points are the computed solutions obtained using $h = 0$ and $h = 0.99$, respectively, with a 200 mesh points.

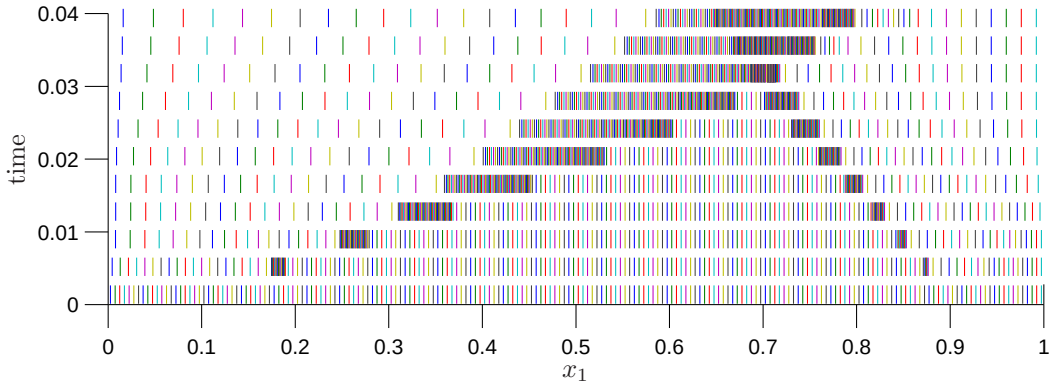

Figure 7: Physical grid coordinates for the generalized Lagrangian run shown in Fig. 6 at eleven different times $t = i \times 0.0038$, for $0, 1, \ldots, 10$. Here the grid system is displayed in the same manner as in Fig. 5.

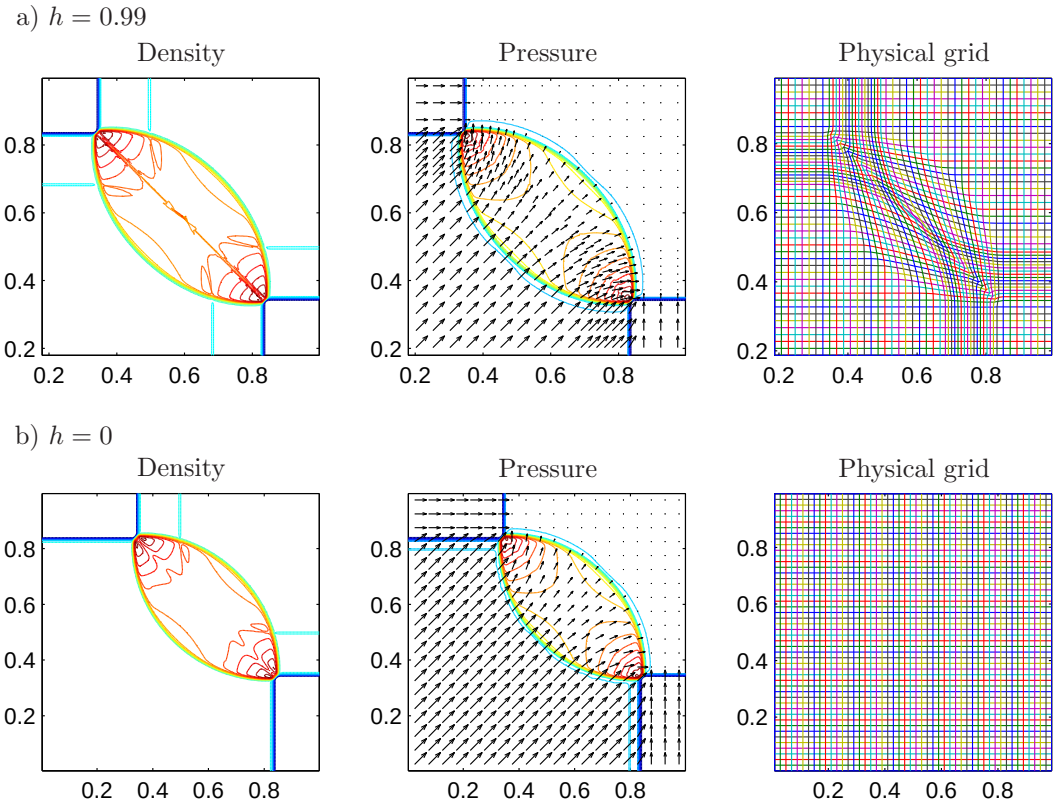

Figure 8: Numerical results for a two-dimensional Riemann problem, a 4-shocks initial condition case. Contour plots of the density and pressure (30 lines range from 0.033 to 1.998 and 0.044 to 2.685, respectively), and the physical grid coordinates are shown at time $t = 0.2$ obtained using both $h = 0$ and 0.99 with a 200×200 grid. Note that the computed velocity field is superimposed into the pressure contours. For clarity, solution coarsening factors of 10 and 4 in each x_1- and x_2-direction are used to graph the velocity vectors and the physical grid system, respectively.

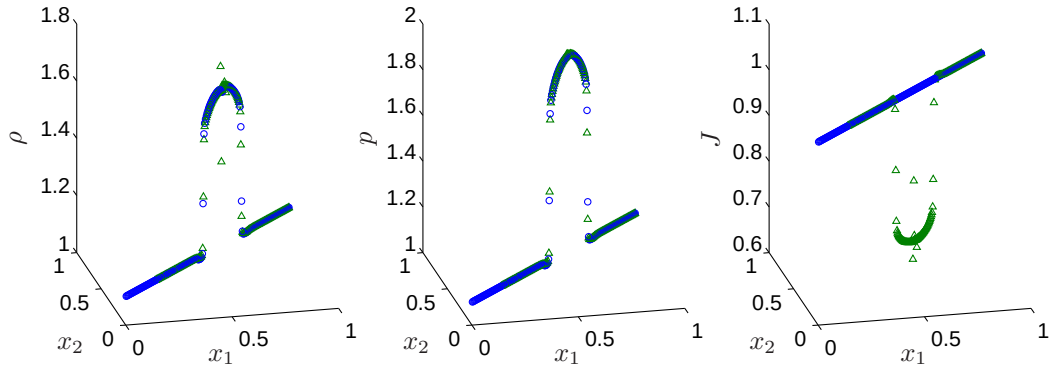

Figure 9: Cross-sectional plots of the results for the shown shown in Fig. 8 along the diagonal axis of the computational grid. The dotted and triangular points are the numerical solutions obtained using $h = 0$ and 0.99, respectively.

for simplicity, we only take a quarter of the unit square domain, *i.e.*, $(x_1, x_2) \in [0, 0.5] \times [0, 0.5]$ m^2, and apply the line of symmetry boundary conditions to the bottom and the left sides during the computations.

Fig. 10 shows contours of the density and pressure, and the physical grid system at time at time $t = 120\mu$s with a 100×100 grid, where the graphs are displayed in the same manner as in Fig. 8. Good resolution of the wave pattern (*i.e.*, both the shock and interface remain circular and appear to be very well located) are easily seen from the contour plots. The scatter plots shown in Fig. 11 provide the validation of our two-dimensional results as in comparison with the "true" solution obtained from solving the one-dimensional model with appropriate source terms for the radial symmetry, using the Eulerian high-resolution method with a 1200 mesh points (cf. [44]). Here $\bar{u} = \sqrt{u_1^2 + u_2^2}$ denotes the radial velocity. From the figure, it is clear that our results agree quite well with the "true" physical solutions, and are free of spurious fluctuations in the pressure near the gas-liquid interface. We also observe some improvement in the density across the interface when the current generalized Lagrangian grid approach is in use as opposed to the standard Eulerian grid approach.

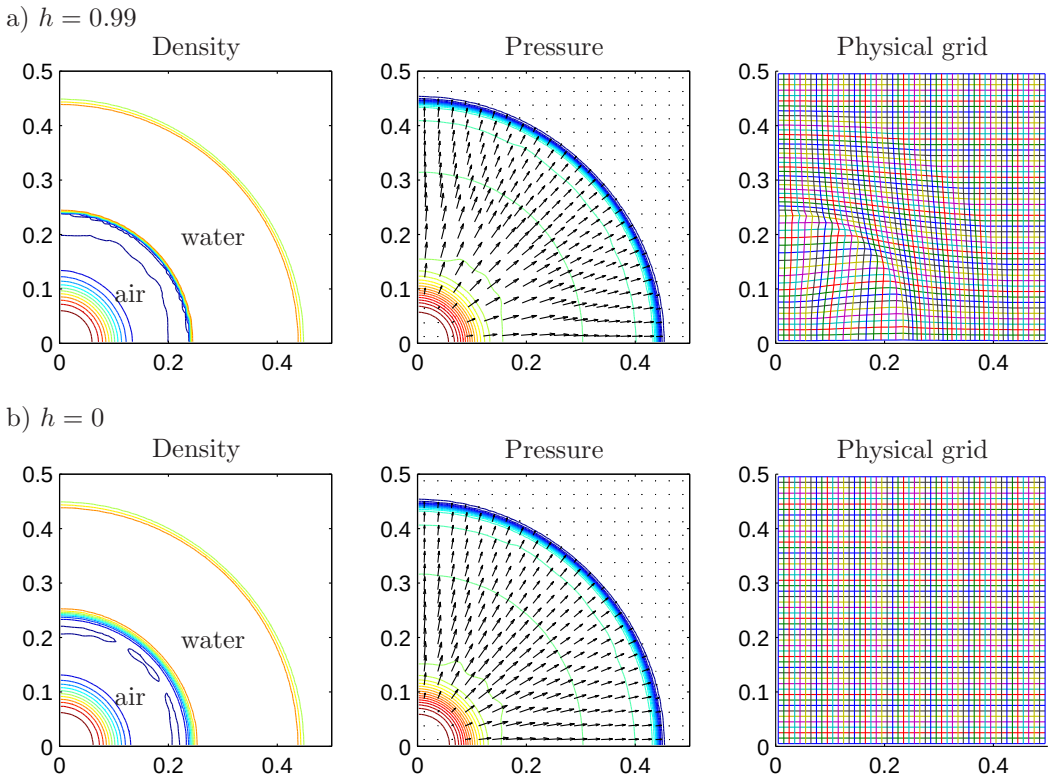

Figure 10: Numerical results for a two-component radially symmetric problem at time $t = 120\mu$s with a 100×100 grid. Here the solutions are plotted in the same manner as in Fig. 8 with the contours ranging from 20.8 to 1270.8 kg/m^3 and 16.7 to 1016MPa, for the density and pressure, respectively.

Example 6.2.3. As an example to show how our algorithm works on interaction between shock wave and material interface, we are interested in a model underwater explosion problem (cf. [12, 47, 50]). In this test, we take a rectangular domain $(x_1, x_2) \in [-2, 2] \times [-1.5, 1]$m^2, and consider the initial condition that is composed of a stationary horizontal air-water interface at the $x_2 = 0$ axis and a circular gas bubble in water with the center $(x_1^0, x_2^0) = (0, -0.3)$m and of the radius $r_0 = 0.12$m. Here above the air-water

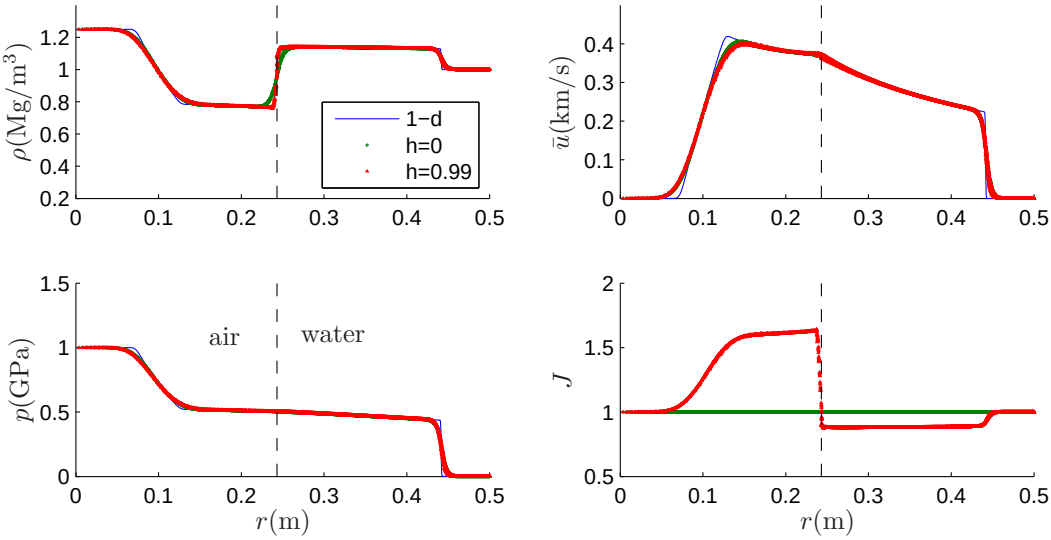

Figure 11: Scatter plots of the results for the run shown in Fig. 10. The solid line is the "true" solution obtained from solving the one-dimensional model with appropriate source terms for the radial symmetry using the high-resolution method and 1200 mesh points. The dotted and triangular points are the two-dimensional results obtained using $h = 0$ and 0.99, respectively. The dashed line is the approximate location of the air-water interface.

interface, the fluid is a perfect gas at the standard atmospheric condition,

$$(\rho,\ u_1,\ u_2,\ p,\ \alpha) = \left(1.2\ \text{kg/m}^3,\ 0,\ 0,\ 10^5\ \text{Pa},\ 1\right).$$

Below the air-water interface, in region inside the gas bubble the fluid is modeled as a perfect gas also with the state variables

$$(\rho,\ u_1,\ u_2,\ p,\ \alpha) = \left(1250\ \text{kg/m}^3,\ 0,\ 0,\ 10^9\ \text{Pa},\ 1\right),$$

and in region outside the gas bubble the fluid is water with the state variables

$$(\rho,\ u_1,\ u_2,\ p,\ \alpha) = \left(10^3\ \text{kg/m}^3,\ 0,\ 0,\ 10^5\ \text{Pa},\ 0\right).$$

There are three solid walls at the left, right, and bottom boundaries in the current problem formulation.

As in Example 6.2.2, breaking of this underwater bubble would results in an outward-going shock wave in water, an inward-going rarefaction wave in gas, and a material interface lying in between that separates the gas and water. Soon after this shock wave is diffracted through the nearby flat air-water interface, it is known in the literature (cf. [12]) that the topology of the underwater bubble will undergo a change from the original circular-shape to an oval-like shape. As time evolves, this gas bubble would continue rising upward, causing the subsequent deformation of the horizontal air-water interface.

Contour plots of the density and pressure at four different times $t = 0.2,\ 0.4,\ 0.8$, and 1.2ms are presented in Fig. 12, where we have performed the computation using $h = 0$ and 0.95 with a 400×250 grid. From the density plot, we clearly observe the improvement on the use of the generalized Lagrangian method over the Eulerian method to the sharpness of the solution structure near the interfaces. Moreover, from the pressure plot, we see the smooth variation of the solution near the interface, without introducing any spurious oscillations. In Fig. 13, we present the physical grid system for the generalized Lagrangian

run shown in Fig. 12 where the dynamical movement of the grids that follow closely to the main feature of the flow is observed. The cross-section of the density and pressure for the same run along line $x_1 = 0$ is drawn in Fig. 14, giving some quantitative information about the differences of the Eulerian and generalized Lagrangian results at the selected times. The time history of the computed grid Jacobian J for the generalized Lagrangian run is plotted in Fig. 15, where J_{ave}, $J_{\min}$, and $J_{\max}$ denote the average, minimum, and maximum values of J, respectively.

To end this section, it should be mentioned that all the simulations done here were run on an AlphaServer DS20E under the Tru64 Unix operating system. As the whole, it is observed that, the CPU time that requires for carrying out the generalized Lagrangian computations depends strongly on the uniformity of the grid structure. Consider the case for the underwater explosion problem in EXAMPLE 6.2.3, for example, it took in turn 695.2253 and 1528.683 seconds for the Eulerian and the Lagrangian run, while for the radially symmetric problem in EXAMPLE 6.2.2 it took 14.6341 and 17.7257 seconds, respectively. We note that the computer programs (written in Fortran 77) used to obtain the results above are available from the author.

7 Conclusion

We have presented a simple moving grid approach for the numerical simulation of compressible homogeneous two-fluid flow problems with a stiffened gas equation of state in more than one space dimension. The algorithm uses a Lagrangian-like condition for the temporal evolution of the underlying grid system, and employs a volume-fraction based model equations in generalized curvilinear coordinates as a basis for the principal motion of the fluid mixture. A set of geometric conservation laws is included in the mathematical formulation of the problem also for an easy computation of the grid metrics that come as a result of the coordinate transformation between the physical and logical grid. A standard high-resolution method based on the f-waves viewpoint is used to solve the proposed model equations with the dimensional-splitting technique included in the method for multidimensional problems. Numerical results presented in this paper demonstrate clearly the feasibility of the approach for a reasonable class of two-fluid problems. Ongoing work is to study more general grid-movement strategy that is required for a class of solid-solid or fluid-solid impact problems (cf. [10]) and problems with complex geometries (cf. [3]).

Acknowledgement

The author would like to thank Professors W.-H. Hui and J.-J. Hu for valuable conversations and help in the early stage of the work presented here. This research was supported in part by National Science Council of Republic of China Grants NSC 93-2115-M-002-010, 94-2115-M-002-016, and 95-2115-M-002-010.

References

[1] D. A. Anderson, J. C. Tannehill, and R. H. Pletcher. *Computational Fluid Mechanics and Heat Transfer*. McGraw-Hill, New York, 1984.

[2] D. Bale, R. J. LeVeque, S. Mitran, and J. A. Rossmanith. A wave propagation method for conservation laws and balance laws with spatially varying flux functions. *SIAM J. Sci. Comput.*, 24:955–978, 2002.

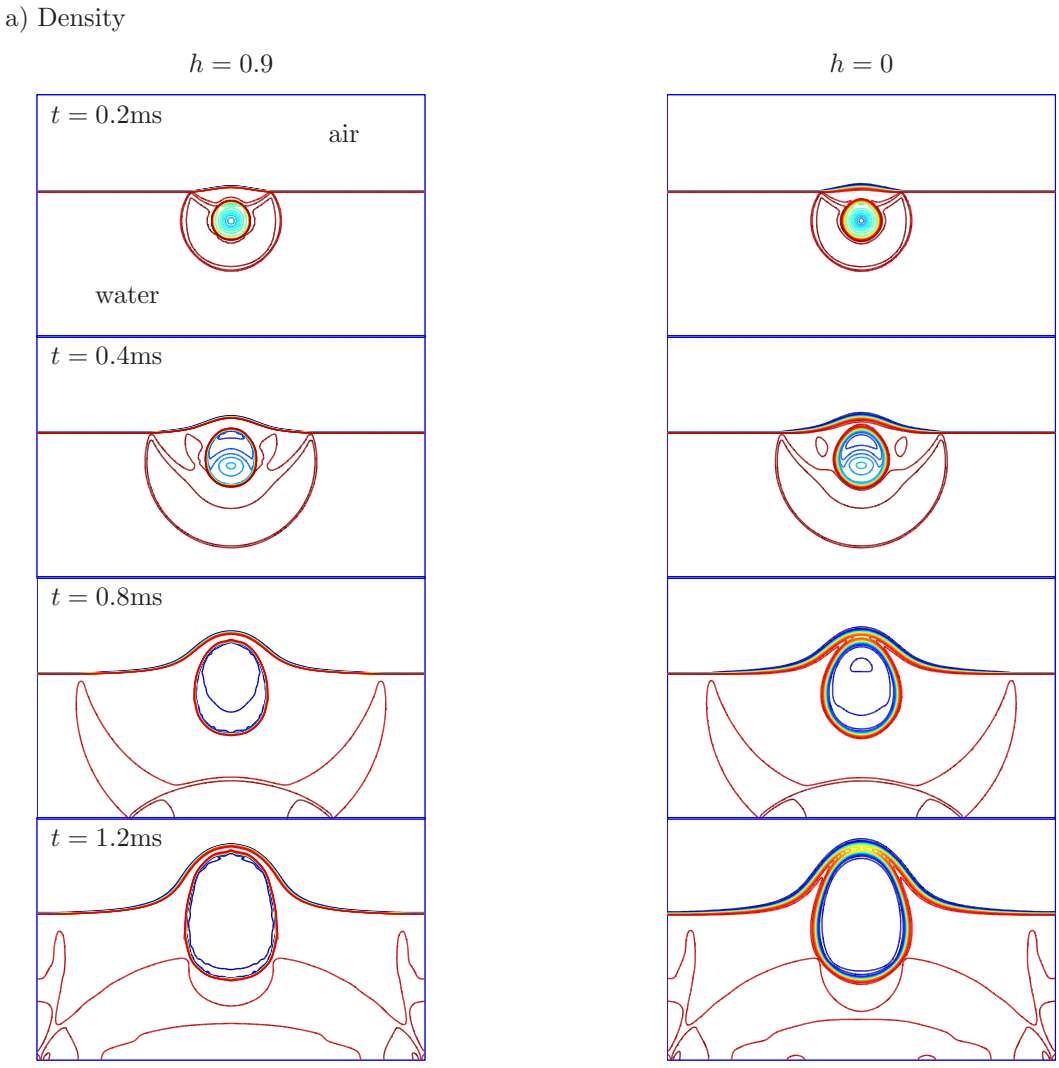

Figure 12: Numerical results for the simulation of a model underwater explosion problem. Contour plots are shown for (a) the density (30 lines range from 18.6 to 1137.2 kg/m^3), and (b) the pressure (30 lines range from 6.43 to 392.18MPa) at four different times $t = 0.2$, 0.4, 0.8, and 1.2ms obtained using both $h = 0$ and 0.95 with a 400×250 grid.

b) Pressure

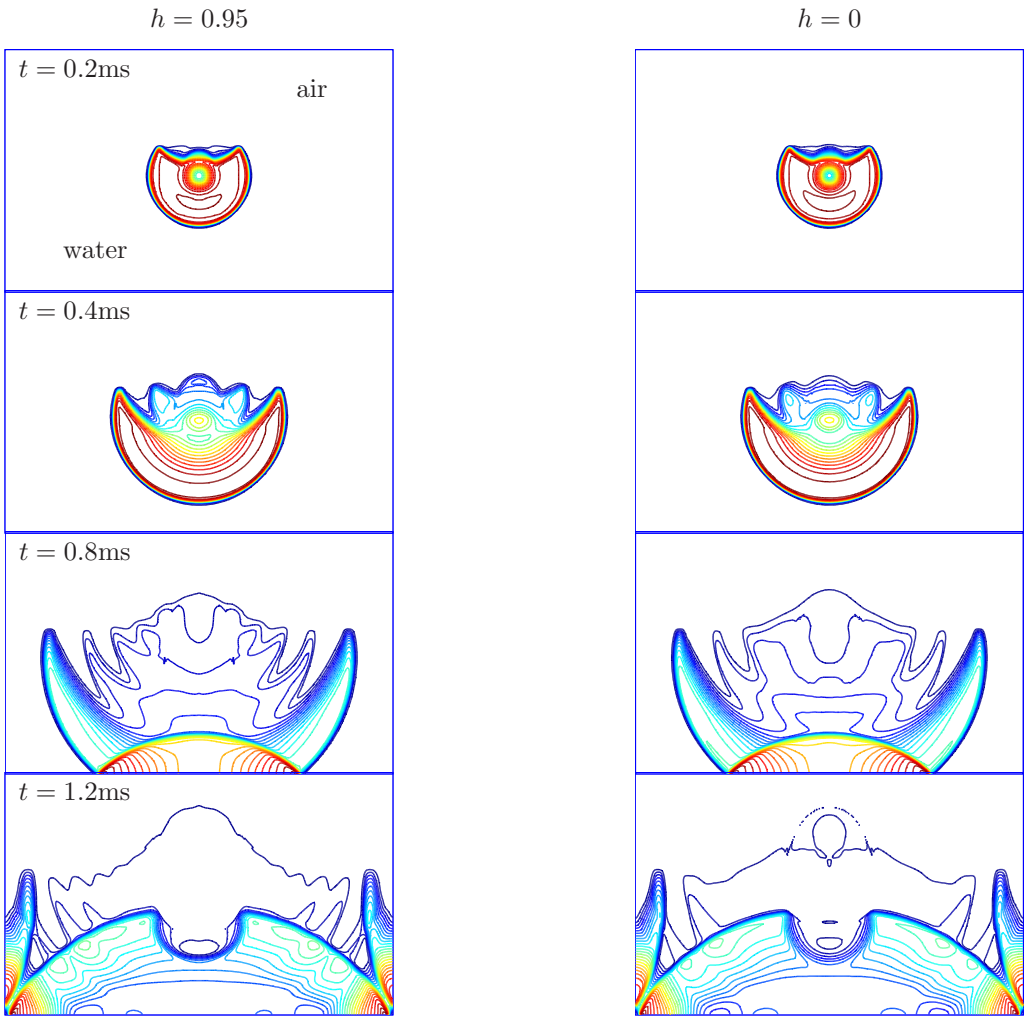

Figure 12: (continued)

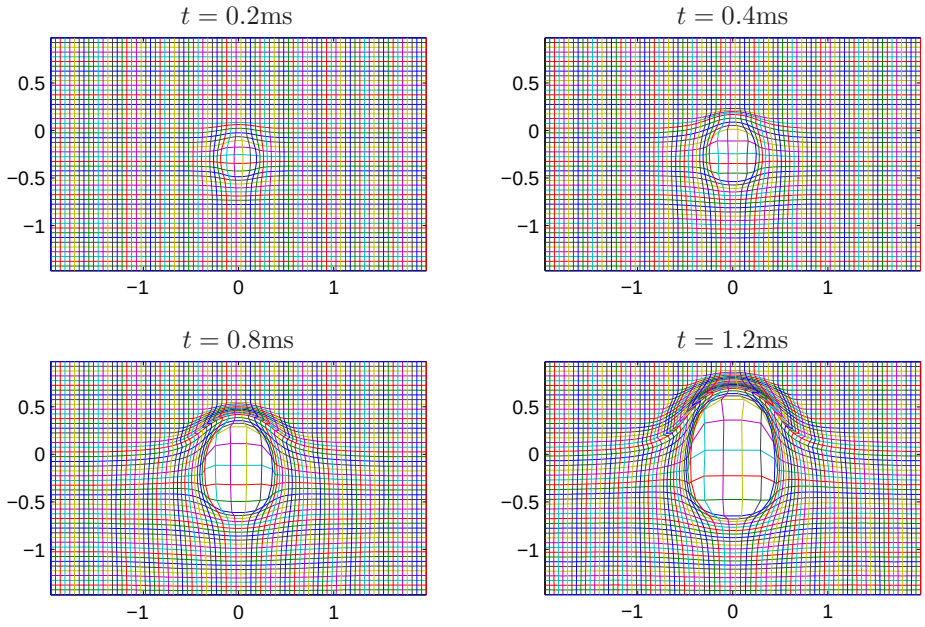

Figure 13: Physical grid system for the generalized Lagrangian run with $h = 0.95$ shown in Fig. 12. For clarity, a grid coarsening factor of 5 in each x_1- and x_2-direction is used to make each of the graphs.

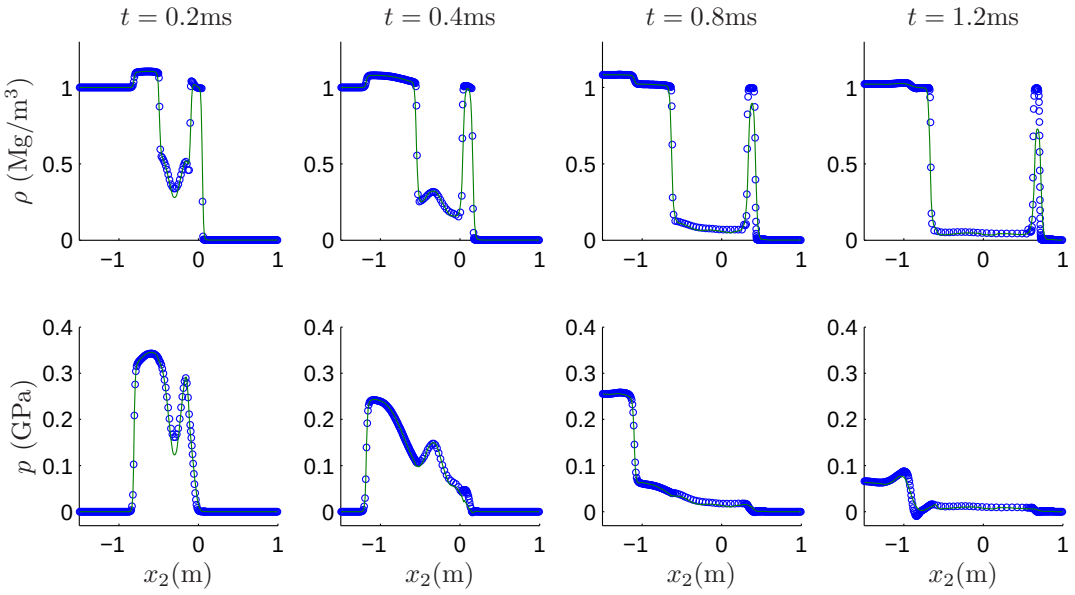

Figure 14: Cross-sectional plots of the results for the run shown in Fig. 12 along $x_1 = 0$, where the solid line and dotted points are the numerical solutions obtained using $h = 0$ and 0.95, respectively.

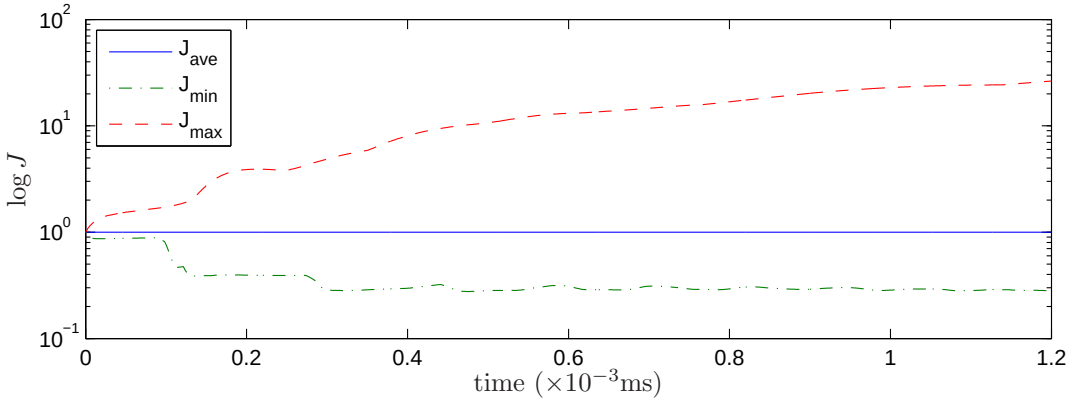

Figure 15: Time history of the grid Jacobian J for the generalized Lagrangian run shown in Fig. 12, where J_{ave}, J_{min}, and J_{max} denote the average, minimum, and maximum values of J, respectively.

[3] J. W. Banks, D. W. Schwendeman, A. K. Kapila, and W. D. Henshaw. A high-resolution Godunov method for compressible multi-material flow on overlapping grids. *J. Comput. Phys.*, Article in Press, 2006.

[4] D. A. Calhoun, C. Helzel, and R. J. LeVeque. Logically rectangular grids and finite volume methods for PDEs in circular and spherical domains. *preprint*, 2006.

[5] J. Cheng and C.-W. Shu. A high order ENO conservative Lagrangian type scheme for the compressible Euler equations. *J. Comput. Phys.*, 227:1567–1596, 2007.

[6] P. Colella. Glimm's method for gas dynamics. *SIAM J. Sci. Stat. Comput.*, 3(1):76–110, 1982.

[7] P. Colella and H. M. Glaz. Efficient solution algorithms for the Riemann problem for real gases. *J. Comput. Phys.*, 59:264–289, 1985.

[8] R. Courant and K. O. Friedrichs. *Supersonic Flow and Shock waves*. Wiley-Interscience, New York, 1948.

[9] B. Despres and C. Mazeran. Lagrangian gas dynamics in two dimensions and Lagrangian systems. *Arch. Rat. Mech. Anal.*, 178:327–372, 2005.

[10] G. R. Gisler, R. P. Weaver, C. L. Mader, and M. L. Gittings. Two- and three-dimensional asteroid impact simulations. *IEEE Computing in Science and Engineering*, May/June:46–55, 2004.

[11] E. Godlewski and P.-A. Raviart. *Numerical Approximation of Hyperbolic Systems of Conservation Laws*. Springer-Verlag, 1996. Applied Mathematical Science 118.

[12] J. Grove and R. Menikoff. The anomalous reflection of a shock wave at a material interface. *J. Fluid Mech.*, 219:313–336, 1990.

[13] B. Gustafsson, H.-O. Kreiss, and J. Oliger. *Time Dependent Problems and Difference Methods*. John Wiley & Sons, Inc., New York, 1995.

[14] A. Harten, P. D. Lax, and B. van Leer. On upstream differencing and Godunov-type schemes for hyperbolic conservation laws. *SIAM Review*, 25:35–61, 1983.

[15] K. A. Hoffmann and S. T. Chiang. *Computational Fluid Dynamics*. Engineering Education System, Wichita, Kansas, USA, 4 edition, 2000.

[16] W. H. Hui. The unified coordinate system in computational fluid dynamics. *Comm. Comput. Phys.*, 2:577–610, 2007.

[17] W. H. Hui and S. Koudriakov. A unified coordinate system for solving the three-dimensional Euler equtions. *J. Comput. Phys.*, 172:235–260, 2001.

[18] W. H. Hui and S. Koudriakov. Computation of the shallow water equations using the unified coordinates. *SIAM J. Sci. Comput.*, 22(5):1615–1654, 2002.

[19] W. H. Hui, P. Y. Li, and Z. W. Li. A unified coordinate system for solving the two-dimensional Euler equtions. *J. Comput. Phys.*, 153:596–637, 1999.

[20] P. Jia, S. Jiang, and G. P. Zhao. Two-dimensional compressible milti-material flow calculations in a unified coordinate system. *Computers and Fluids*, 35:168–188, 2006.

[21] C. Jin and K. Xu. A unified moving grid gas-kinetic method in Eulerian space for viscous flow computation. *J. Comput. Phys.*, 222:155–175, 2007.

[22] D. Kincaid and W. Cheney. *Numerical Analysis*. Brooks/Cole, 1990.

[23] H.-O. Kreiss and J. Lorenz. *Initial-Boundary Value Problems and Navier-Stokes Equations*. Academic Press, San Diego, 1989.

[24] A. G. Kulikovskii, N. V. Pogorelov, and A. Yu. Semenov. *Mathematical aspects of Numerical Solution of Hyperbolic Systems*. Chapman & Hall/CRC, Boca Raton, 2001.

[25] R. J. LeVeque. *Numerical Methods for Conservation Laws*. Birkhäuser-Verlag, 2 edition, 1992.

[26] R. J. LeVeque. *Finite Volume Methods for Hyperbolic Problems*. Cambridge University Press, 2002.

[27] R. J. LeVeque and K.-M. Shyue. One-dimensional front tracking based on high resolution wave propagation methods. *SIAM J. Sci. Comput.*, 16:348–377, 1995.

[28] M.-S. Liou. An extended Lagrangian method. *J. Comput. Phys.*, 118:294–309, 1995.

[29] H. Luo, J. D. Baum, and R. Löhner. On the computation of multi-material flows using ALE formulation. *J. Comput. Phys.*, 194:304–328, 2004.

[30] P.-H. Maire, R. Abgrall, J. Breil, and J. Ovadia. A cell-centered Lagrangian scheme for two-dimensional compressible flow problems. *SIAM J. Sci. Comput.*, 29:1781–1824, 2007.

[31] S. P. Marsh. *LASL Shock Hugoniot Data*. University of California Press, Berkeley, 1980.

[32] D. J. Mavriplis and Z. Yang. Construction of the discrete geometric conservation law for high-order time-accurate simulations on dynamic meshes. *J. Comput. Phys.*, 213:557–573, 2006.

[33] H. J. Melosh. *Impact Cratering: A Geologic Process*. Oxford University Press, 1989.

[34] R. Menikoff and B. Plohr. The Riemann problem for fluid flow of real materials. *Rev. Mod. Phys.*, 61:75–130, 1989.

[35] J. Morrell. *A cell by cell adaptive mesh Lagrangian scheme for the numerical solution of the Euler equations.* Numerical Analysis Report 1/05, Department of Mathematics, University of Reading, May, 2005 (unpublished). Available at the URL http://www.maths.rdg.ac.uk/research/publications/NA-reports/01-05.pdf.

[36] D. Rochette and S. Clain. Two-dimensional computation of gas flow in a porous bed characterized by a porosity jump. *J. Comput. Phys.*, 219:104–119, 2006.

[37] D. Rochette, S. Clain, and T. Buffard. Numerical scheme to complete a compressible gas flow in variable porosity media. *Int. J. Comput. Fluid Dyn.*, 19(4):299–309, 2005.

[38] P. L. Roe. Approximate Riemann solvers, parameter vector, and difference scheme. *J. Comput. Phys.*, 43:357–372, 1981.

[39] J. A. Rossmanith. A wave propagation method for hyperbolic systems on the sphere. *J. Comput. Phys.*, 213:629–658, 2006.

[40] J. A. Rossmanith, D. Bale, and R. J. LeVeque. A wave propagation algorithm for hyperbolic systems on curved manifolds. *J. Comput. Phys.*, 199:631–662, 2004.

[41] R. Saurel, J. Massoni, and F. Renaud. A numerical method for one-dimensional compressible multiphase flow on moving meshes. *Int. J. Numer. Meth. Fluids*, 54(12):1425–1450, 2007.

[42] C. W. Schulz-Rinne, J. P. Collins, and H. M. Glaz. Numerical solution of the Riemann problem for two-dimensional gas dynamics. *SIAM J. Sci. Comput.*, 14:1394–1414, 1993.

[43] M. Shashkov and B. Wendroff. A composite scheme for gas dynamics in Lagrangian coordinates. *J. Comput. Phys.*, 150:502–517, 1999.

[44] K.-M. Shyue. An efficient shock-capturing algorithm for compressible multicomponent problems. *J. Comput. Phys.*, 142:208–242, 1998.

[45] K.-M. Shyue. A fluid-mixture type algorithm for compressible multicomponent flow with van der Waals equation of state. *J. Comput. Phys.*, 156:43–88, 1999.

[46] K.-M. Shyue. A fluid-mixture type algorithm for compressible multicomponent flow with Mie-Grueneisen equation of state. *J. Comput. Phys.*, 171:678–707, 2001.

[47] K.-M. Shyue. A simple volume tracking method for compressible two-phase flow. *J. Korean Astro. Soc.*, 34:S237–241, 2001.

[48] K.-M. Shyue. A fluid-mixture type algorithm for barotropic two-fluid flow problems. *J. Comput. Phys.*, 200:718–748, 2004.

[49] K.-M. Shyue. A volume-fraction based algorithm for hybrid barotropic and non-barotropic two-fluid flow problems. *Shock Waves*, 15(6):407–423, 2006.

[50] K.-M. Shyue. A wave-propagation based volume tracking method for compressible multicomponent flow in two space dimensions. *J. Comput. Phys.*, 215:219–244, 2006.

[51] J. Smoller. *Shock Waves and Reaction-Diffusion Equations.* Springer-Verlag, New York, 1982.

[52] G. Strang. *Linear Algebra and its Applications.* Thomson, Brooks/Cole, Belmont, CA, USA, 2006.

[53] P. D. Thomas and C. K. Lombard. The geometric conservation law– a link between finite-difference and finite-volume methods of flow computation on moving grids. *AIAA papers CP-78-1208*, 1978.

[54] J. F. Thompson, B. K. Soni, and N. P. Weatherill. *Handbook of Grid Generation.* CRC Press, 1999.

[55] E. F. Toro. *Riemann Solvers and Numerical Methods for Fluid Dynamics: A Practical Introduction, 2nd Edition.* Springer-Verlag, 1999.

[56] P. Woodward and P. Colella. The numerical simulation of two-dimensional fluid flow with strong shock. *J. Comput. Phys.*, 54(1):115–173, 1984.

[57] P. Woodward and P. Colella. The piece-wise parabolic method (PPM) for gas dynamical simulations. *J. Comput. Phys.*, 54:174–201, 1984.